CO_2-Plume Geothermal (CPG) after enhanced oil recovery (EOR)

Kucuk, S.; Farajzadeh, R.; Brehme, M.; Rossen, W. R.; Saar, M. O.

DOI
10.1016/j.geoen.2025.214261

Publication date
2025

Document Version
Final published version

Published in
Geoenergy Science and Engineering

Citation (APA)
Kucuk, S., Farajzadeh, R., Brehme, M., Rossen, W. R., & Saar, M. O. (2025). CO_2-Plume Geothermal (CPG) after enhanced oil recovery (EOR). *Geoenergy Science and Engineering*, *257*, Article 214261. https://doi.org/10.1016/j.geoen.2025.214261

257 (2026) 214261

Contents lists available at ScienceDirect

Geoenergy Science and Engineering

journal homepage: www.sciencedirect.com/journal/geoenergy-science-and-engineering

CO_2-Plume Geothermal (CPG) after enhanced oil recovery (EOR)

S. Kucuk [a,*], R. Farajzadeh [b], M. Brehme [a], W.R. Rossen [b], M.O. Saar [a]

[a] Geothermal Energy and Geofluids Group, Department of Earth and Planetary Sciences, ETH Zurich, Zurich, 8001, Switzerland
[b] Department of Geoscience and Engineering, Delft University of Technology, Stevinweg 1, 2628CN, Delft, The Netherlands

ARTICLE INFO

Keywords:
CO_2 utilization and sequestration
Geothermal energy
CPG
EOR

ABSTRACT

The global energy transition requires novel carbon utilization methods to enable integrated and optimized low-carbon energy production. Coupling CO_2-based geothermal energy extraction with CO_2-enhanced oil recovery (EOR) represents a promising yet largely unexplored approach for improving resource efficiency and carbon sequestration. This study investigates the integration of CO_2-Plume Geothermal (CPG) energy production with CO_2-EOR in mature oil reservoirs using numerical simulations of conceptual heterogeneous reservoir models. The interplay between EOR and CPG performance in terms of energy production and CO_2 storage is evaluated and compared to understand the geotechnical implications of this integration. The analysis highlights that initiating CPG operations after EOR significantly benefits from the established CO_2 plume, facilitating immediate and efficient geothermal energy extraction. Results show that integrating CPG with EOR increases total energy recovery by 20%–50% relative to the energy produced by EOR alone, yielding CPG thermal power outputs ranging from 13 to 23 MW_{th}/km^2. Continued CO_2 injection during CPG operations further increases total CO_2 storage by 80%–280%, driven primarily by improved volumetric sweep of previously unswept reservoir volumes and enhanced CO_2 density resulting from reservoir cooling. While reservoir heterogeneity strongly influences oil recovery during EOR, its effect on CPG thermal output is less pronounced, since native reservoir fluids (oil and brine) have already been largely displaced during the EOR stage, and the CO_2 plume gradually stabilizes over time. These findings demonstrate the viability and advantages of integrated CO_2-EOR and CPG systems, offering insights into novel methods essential for sustainable subsurface resource management and climate-change mitigation.

1. Introduction

The gradual increase in global surface temperature, referred to as global warming, is mainly attributed to the accumulation of greenhouse gases, such as carbon dioxide (CO_2), in Earth's atmosphere (IPCC, 2022). Capturing CO_2 from the atmosphere or directly from emission sources and storing it in deep geologic formations – known as Carbon Capture and Storage (CCS) – has emerged as a pivotal strategy for achieving the global decarbonization goals to mitigate the impact of climate change. However, the combined capacity of existing, under-developed, and planned CCS facilities is still only a small fraction of what is required to meet climate targets (Institute, 2021). Given the economic challenges associated with CCS, which hinder the financial investment needed for its broad implementation, innovative approaches are essential to commercialize current carbon storage schemes and facilitate the widespread deployment of large-scale CCS projects.

Following its capture, CO_2 can be considered a valuable resource, rather than merely a waste product that requires disposal. This perspective, known as Carbon Capture, Utilization, and Storage (CCUS), involves capturing CO_2 through different mechanisms and generating additional economic benefits (Orr, 2018; IEA, 2021), prior to its permanent disposal. Current research on the subsurface utilization of CO_2 focuses primarily on two main applications: (1) increasing oil recovery from mature hydrocarbon fields by injection of miscible CO_2 into the reservoir (also known as CO_2 enhanced oil recovery, or CO_2-EOR), and (2) utilizing CO_2 as the subsurface working fluid for the extraction of geothermal energy, both of which permanently store CO_2 in deep geological formations. However, these methods are typically considered and studied independently, overlooking the potential benefits and/or challenges of coupling them. For instance, extracting geothermal energy using CO2 as a working fluid from hydrocarbon reservoirs where CO_2-EOR was conducted would enable the use of the already established CO_2 plume in the subsurface, existing CO_2-suitable

* Corresponding author.
E-mail addresses: serhat.kucuk@eaps.ethz.ch (S. Kucuk), rouhi@tudelft.nd (R. Farajzadeh), mbrehme@ethz.ch (M. Brehme), rossen@tudelft.nd (W.R. Rossen), saarm@ethz.ch (M.O. Saar).

https://doi.org/10.1016/j.geoen.2025.214261
Received 16 April 2025; Received in revised form 26 August 2025; Accepted 19 October 2025
Available online 22 October 2025

wellbores, and much of the infrastructure on site. This approach could potentially improve the sustainability and economic viability of subsurface applications of CCUS. However, to the best of our knowledge, there has not yet been comprehensive research investigating the potential of this integrated approach.

One particular CO_2 utilization method was introduced and named by Randolph and Saar in 2011 (Randolph and Saar, 2011), namely CO_2-Plume Geothermal (CPG). The CPG technology combines geothermal energy extraction with CO_2 storage in deep (>2 km) geological formations, thereby reducing CO_2 emissions to the atmosphere and thus contributing to mitigating global warming (Randolph and Saar, 2011; Zhang et al., 2014; Garapati et al., 2014, 2015; Adams et al., 2014, 2015; Ezekiel et al., 2020). CPG is added to CCS operations and involves injecting CO_2 into naturally porous and permeable sedimentary reservoirs, such as deep saline aquifers or hydrocarbon reservoirs, to extract geothermal energy. As the produced CO_2 is reinjected into the CO_2 storage formation after giving up energy in a heat exchanger or turbine, the CO_2 is ultimately stored in the deep geologic reservoir, resulting in CO_2 Capture, Utilization and Storage (CCUS).

The literature extensively discusses the advantages of using CO_2 as the working geofluid over water to extract geothermal energy (Brown, 2000; Pruess and Azaroual, 2006; Esteves et al., 2019; Zhong et al., 2023), particularly when used in naturally permeable formations, as opposed to usage in Enhanced Geothermal Systems (EGS) as shown in Fig. 3 in Randolph and Saar (2011). The main reason for the often improved performance of CO_2 over water is that supercritical CO_2 exhibits a significantly lower kinematic viscosity than water under typical reservoir conditions at 2–5 km depth. This lower viscosity allows for increased fluid mass flow rates due to reduced frictional losses within the reservoir, resulting in higher rates of heat extraction, despite CO_2 having a lower heat capacity than water (Randolph and Saar, 2011; Adams et al., 2014). Moreover, because CO_2 has a higher thermal expansivity compared to water, its density is more sensitive to temperature variations. This characteristic leads to the establishment of significant buoyancy-driven thermosiphon flow between injection and production wells, potentially reducing or even eliminating the need for costly pumping (Atrens et al., 2009; Adams et al., 2014, 2015).

CPG systems in deep saline aquifers have been extensively studied. For instance, in addition to the above-cited CPG publications, Garapati et al. (2015) explored the performance in terms of energy extraction and reservoir heat depletion of CO_2-limited CPG systems and for the first time investigated brine displacement by the CO_2 during CPG operations as well as the use of a horizontal production well. Adams et al. (2021) analyzed heat depletion during CPG operations in homogeneous sedimentary basin aquifers and evaluated net electric power generation under varying reservoir and wellbore conditions. Rangel-Jurado et al. (2025) investigated the reduced chemical reactivity of supercritical CO_2, even when saturated with water, highlighting its potential as a superior heat extraction fluid compared to aqueous solutions. Hau et al. (2025) demonstrated that integrating CPG operations with conventional CCS enhances CO_2 sequestration efficiency, improves CO_2 plume control, and provides a stable source of geothermal energy, using field-data-constrained simulations of the Aquistore CCS reservoir over a 30-year period. Studies have also demonstrated that reservoir heterogeneity significantly impacts the performance and energy output of both water-based and CPG systems (Zhang et al., 2021; Norouzi et al., 2022, 2023; Rangel-Jurado et al., 2023). More recently, studies have optimized the surface equipment of CPG systems (Schifflechner et al., 2024), and provided techno-economic analyses of CPG and other CO_2-based geothermal power plants (Rangel-Jurado et al., 2022). Lastly, even though implementing CPG in depleted gas reservoirs has been investigated (Cui et al., 2016; Ezekiel et al., 2020), the potential of CPG in oil reservoirs remains largely unexplored.

Another well-recognized and extensively studied utilization of CO_2 is enhanced oil recovery (EOR) (IEA, 2015; Lake et al., 2019), which targets the significant amount of residual oil left in the reservoir after primary and secondary recovery stages (e.g., waterflooding and CO_2 flooding). In a typical CO_2-EOR process, CO_2 dissolves in crude oil, causing it to swell and reducing its viscosity, which enhances its flow within the reservoir. Simultaneously, light hydrocarbon components dissolve into the CO_2-rich phase, facilitating their production at the wellbore (Stalkup, 1983). When the pressure exceeds the minimum miscibility pressure (MMP), a single-phase oil/CO_2 mixture forms, further improving displacement efficiency and enabling enhanced oil recovery at the production well (Stalkup, 1983; Pedersen et al., 2015).

The literature extensively addresses various aspects of CO_2-EOR operations, with a primary focus on optimizing oil recovery (Alvarado and Manrique, 2010; Karimov and Toktarbay, 2024). More recently, researchers have recognized its potential for long-term carbon storage, exploring CO_2-EOR as a dual-purpose method for oil recovery and carbon sequestration (Ampomah et al., 2017; Farajzadeh et al., 2020). Significant amounts of subsurface-injected CO_2 become trapped in geological formations through various mechanisms such as dissolution, capillary, and structural trapping. Numerous studies have assessed the net carbon balance by comparing CO_2 emissions from oil consumption and other field activities with the amount of CO_2 permanently stored through CO_2-EOR (Aycaguer et al., 2001; Núñez-López and Moskal, 2019; Farajzadeh et al., 2020).

Although the geothermal potential of oil reservoirs has been explored in various contexts, its integration with CO_2-EOR operations, particularly when using CO_2 as the subsurface geothermal working fluid, remains unexplored. Several studies have evaluated the geothermal resource potential of oil fields (Erdlac et al., 2007; Soldo et al., 2020; Huang et al., 2022), including converting oil wells into geothermal wells using downhole heat exchangers (Shmeleva, 2018; Singh, 2020) and generating geothermal electricity from co-produced hot brine (Milliken, 2007; Li et al., 2014; Kharseh et al., 2015; Liu et al., 2018). Furthermore, in-situ oil combustion for geothermal power generation has been explored (Zhu et al., 2019). However, to the best of our knowledge, no study has yet examined the use of CO_2 as a geothermal working fluid in oil fields following CO_2-EOR operations, while accounting for prior field activity and the effects of reservoir permeability heterogeneity.

Therefore, this study explores the geotechnical viability of implementing CPG energy systems in oil fields that have undergone CO_2-EOR operations. We start by generating reservoir model realizations with permeability heterogeneities to simulate the movement of the CO_2 plume under typical reservoir conditions. These models account for critical factors, such as CO_2 channeling through high-permeability sections, a common issue in EOR operations which can diminish oil recovery rates, and evaluate its impact on the performance of the associated CPG system.

We employ multi-phase, full-physics flow simulations that account for compositional and thermal effects while incorporating the oil field's operational history, including waterflooding. This integrated modeling approach is crucial for accurately assessing system performance. Each operational stage's initial conditions depend on the final conditions of the preceding stage, which are influenced by both geological and operational factors.

Next, we validate the EOR performance of the conceptual oil field models against publicly available data. We then evaluate the geothermal power production rates of the CPG system and compare these rates with the energy production achieved during the EOR phase.

Finally, to quantify the additional benefits of integrating these two techniques, we analyze and compare the CO_2 utilization factors. This includes estimating the CO_2 sequestration rates during both stages and calculating the amount of energy produced per unit of CO_2 geologically sequestered.

This study addresses a critical gap in understanding the integration of CO_2-Plume Geothermal (CPG) energy production after enhanced oil recovery in oil reservoirs. By investigating the geotechnical feasibility of this combined approach, our research can offer insights that are

expected to pave the way for further investigations into the economic implications and overall system optimization for energy generation.

Additionally, our findings could promote the use of geothermal energy as a sustainable approach to CO_2 sequestration in oil fields. This may help shape policy decisions while encouraging more efficient and economically viable CO_2 Capture, Utilization, and Storage (CCUS) operations.

2. Methodology

This section outlines the methodology employed to assess the potential of CPG energy production in oil reservoirs, integrated with CO_2-EOR operations.

The initial step involves creating various geologic reservoir model realizations with different degrees of reservoir heterogeneity, focusing solely on the spatial variation of permeability. These models are designed to simulate key processes observed in field applications, such as CO_2 channeling through high-permeability sections of the reservoir, viscous fingering due to the mobility contrast between CO_2 and native reservoir fluids, and gravity override, caused by fluid density differences. These phenomena influence several critical factors, including the sweep efficiency of the CO_2 plume, CO_2 mass flow rates, and CO_2 and thermal breakthrough times. They ultimately affect the incremental oil recovery during the EOR operation and the heat extraction performance during the CPG operation. In this context, sweep efficiency refers to the *volumetric* sweep of the reservoir rock by supercritical CO_2, assuming ideal *displacement* efficiency under miscible conditions (Holm and Josendal, 1974; Lee and Kam, 2013).

The following sections provide an in-depth discussion of the static geological models utilized, outline the operational stages employed during the numerical simulations, and detail the properties and parameters applied in the simulations.

2.1. Static geologic models

We use conceptual oil reservoirs represented by numerical three-dimensional (3D) geologic models generated employing a stochastic approach. Each model has a reservoir footprint of 1 × 1 km^2 and a thickness of 50 m. Other reservoir properties are summarized in Table 1.

The reservoir models are assumed to be initially hydrostatically pressured and geothermally heated (under uniform gradients of 0.1 bar/m and 0.034 °C/m, respectively). Under initial conditions, the reservoir pore space is assumed to be fully saturated with oil and connate formation water.

An inverted five-spot well configuration is employed, utilizing symmetry to effectively simulate only one-quarter of the model's area (Pruess, 2006; Pan et al., 2016; Ezekiel et al., 2020; Kutsienyo et al., 2021), as illustrated in Fig. 1. Both the injector and producer wells are designed with perforations spanning the entire thickness of the model.

No-fluid-flow boundary conditions are defined at the top and bottom layers of the model, indicating that it is overlain by an impermeable caprock, and underlain by a seal rock. Similarly, the lateral boundaries are treated as no-flow zones due to symmetry with the adjacent inverted five-spot well patterns. Vertical heat transfer at the top and bottom boundaries to the surrounding rock is accounted for (see Section 2.3).

2.1.1. Geostatistical generation of heterogeneous reservoir models

Spatially varying permeability fields were generated to represent reservoir heterogeneity while accounting for the spatial correlation (or continuity) of permeability values. A three-dimensional Gaussian Random Field Simulator (GRFS), developed by Räss et al. (2019), was used to create heterogeneous permeability fields under the assumption that the logarithm of rock permeability follows a normal (Gaussian) distribution (Robin et al., 1993; Nick et al., 2009; Taheriotaghsara et al., 2020; Li et al., 2022). The GRFS tool utilizes user-defined input parameters (Table 1), including correlation lengths in the x, y, and z directions and the standard deviation of the Gaussian random field (in base-10 log units), to generate a coherent 3D parameter space for log-permeability across all spatial dimensions (Räss et al., 2019).

Table 1
Key reservoir properties and input parameters for geostatistical permeability-field generation.

Reservoir properties		
Property	Value	Units
Reservoir depth	3000	m
Reservoir footprint (areal)	1	km^2
Reservoir thickness	50	m
Mean annual surface temperature	15	°C
Geothermal gradient	0.034	°C/m
Reservoir initial temperature	120	°C
Reservoir initial pressure	300	bar
Rock density	2650	kg/m^3
Rock thermal conductivity	2.3	W/m/°C
Rock specific heat capacity	1000	J/kg/°C
Connate water saturation	0.20	–
Porosity	0.20	–
Permeability (geometric mean)	10[a]	mD
Ratio of vertical to horizontal permeability	0.2	–
Input for geostatistical (log)permeability-field generation		
Property	Value	Units
Lateral correlation length	700	m
Vertical correlation length	5, 10	m
Standard deviation	1.5	–
Number of realizations	20	–

[a] The geometric mean of the reservoir permeability in geostatistically generated heterogeneous models.

The simulator employs an exponential covariance function, as detailed by Algorithm 1 in Raess et al. (2019). A minor modification was made in this study to adjust the geometric mean of the generated random field, originally set to 0, to ensure a log(k) mean value corresponding to approximately 10 mD (Fig. 1).

We generated twenty realizations of permeability fields to represent various heterogeneous oil fields (Fig. 1). The lateral correlation length was set to 707 m, matching the distance between the injector and producer in the well pattern, to simulate a "layer-cake" lithology. While a more detailed analysis could incorporate variations in mineralogy, rock classes, and their associated properties, our study focuses on permeability variations as the primary representation of heterogeneity within the layer. All other parameters were kept consistent with those listed in Table 1.

2.2. Operational stages

Oil fields typically undergo multiple stages of development over their production lifespan. During the primary recovery stage, oil is brought to the surface using the reservoir's natural pressure, gravity, gas cap (if present), artificial lifting methods, or a combination of these (Ahmed, 2007). However, oil recovery during this stage is relatively low, typically ranging from 5% to 15% of the original oil in place (OOIP) (Christiensen et al., 2001). Following primary recovery, secondary recovery methods are employed, with waterflooding being the most commonly used technique (Ahmed, 2007; Lake et al., 2014; Lyons et al., 2016). While these two stages are widely applied and share similarities in approach and methodology, they often leave a substantial portion of the OOIP unrecovered (Morrow, 1990). To extract additional oil that cannot be recovered through primary or secondary methods, tertiary (or enhanced) oil recovery (EOR) techniques are used. Among these, miscible gas injection, particularly using CO_2, is one of the most widely employed methods (Johns and Dindoruk, 2013).

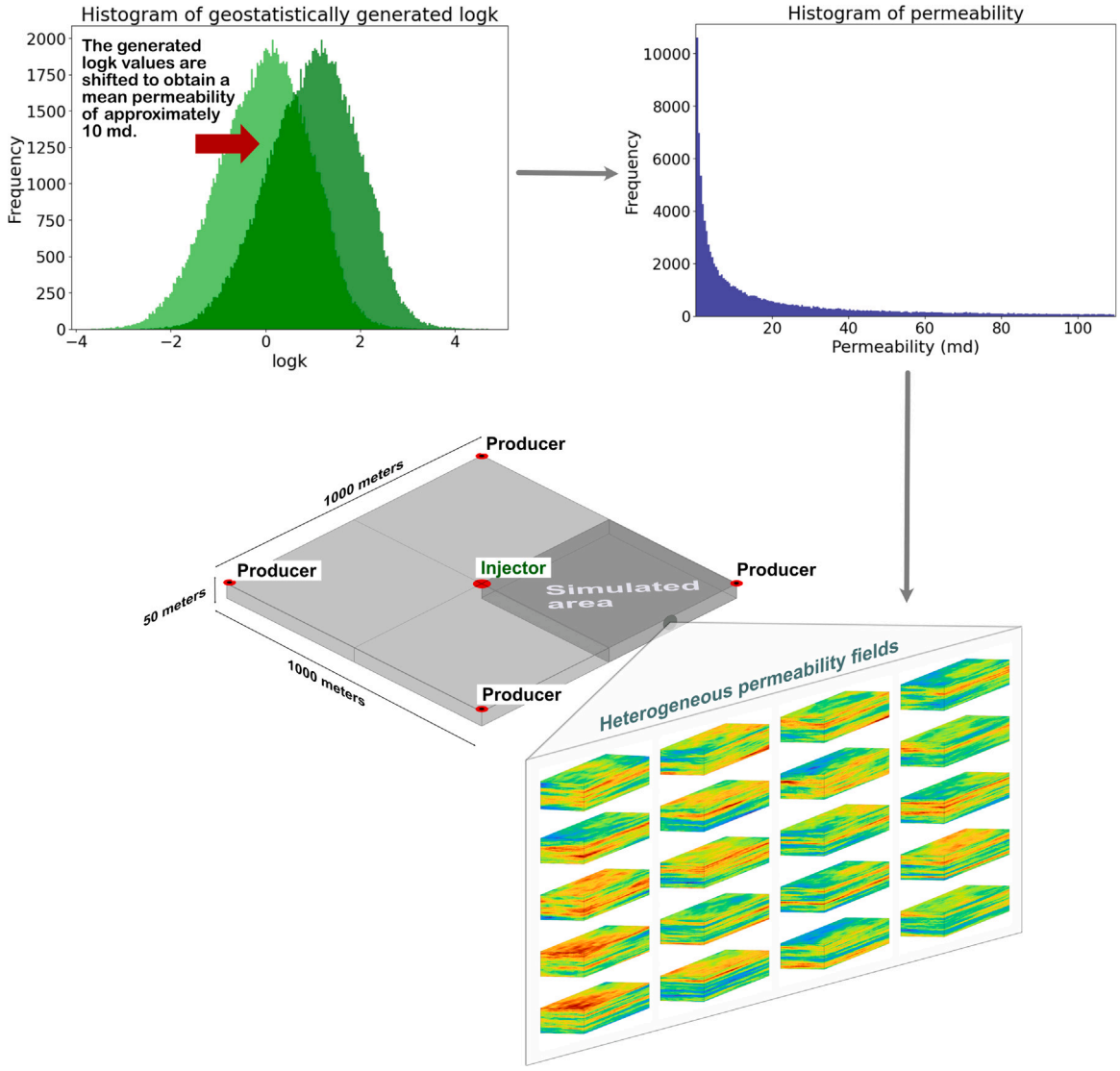

Fig. 1. Visualization of the geostatistical process used to generate heterogeneous reservoir models. The left plot shows an example histogram of geostatistically generated log-k values, adjusted to achieve a geometric mean permeability of 10 mD. The middle plot shows the corresponding permeability (k) histogram. The right panel depicts the inverted 5-spot well pattern for a 1 km × 1 km area and the 20 heterogeneous permeability fields created using this method. The detailed geostatistical procedure is described in Section 2.1.1.

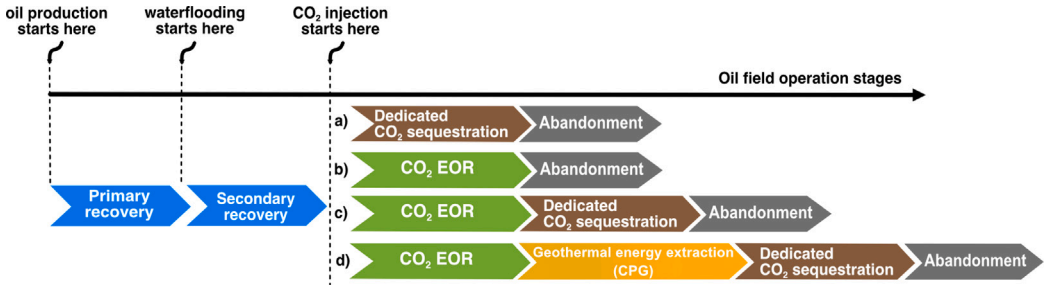

Fig. 2. Typical oil field development stages and possible operations during CO_2 injection after primary and secondary oil recovery. Our study focuses on integrating a CPG energy production stage (Option d), following CO_2-EOR, in mature oil fields, excluding dedicated CO_2 sequestration, which is beyond the scope of our study.

Fig. 2 illustrates the potential development stages of typical oil fields undergoing CO_2 injection (a–d). If recovering the remaining oil is economically or technically unfeasible, the reservoir can be repurposed solely for CO_2 sequestration (Option a). Another option involves utilizing CO_2 injection as an EOR technique to enhance ultimate oil recovery. A third option combines these approaches, starting with CO_2-EOR and transitioning to dedicated carbon sequestration after oil recovery is complete. In this study, we propose further extending the operational lifespan of the field by integrating a CO_2-Plume Geothermal (CPG) stage, which produces CO_2-based geothermal energy following CO_2-EOR (Option d).

Our simulations include primary and secondary oil recovery stages, CO_2-EOR, and CPG operations, employing an integrated modeling approach. This approach ensures that the initial conditions of each stage are informed by the final conditions of the preceding stage (e.g., in Option d, the reservoir state at the end of CO_2-EOR sets the starting conditions for the CPG stage, accounting for various factors, including reservoir heterogeneity). Details of the numerical simulation settings are presented in the next section.

2.3. Numerical simulation

We use the Generalized Equation-of-State Modeling (GEM) software from the Computer Modeling Group (Computer Modeling Group, 2024b) to perform non-isothermal, multi-component flow and transport simulations. GEM is a highly efficient, multidimensional compositional simulator, based on an equation-of-state (EOS) framework. It is capable of modeling the critical mechanisms involved in miscible gas injection processes, including oil swelling, gas condensation, viscosity alterations, interfacial tension changes, and miscibility. The following sections describe the mathematical and physical framework applied in the numerical simulations.

2.3.1. Governing equations and fluid modeling

The flow of fluids in porous media is governed by Darcy's law, combined with the mass balance of components in the oil, gas, and water phases. The mass balance accounts for porosity, phase molar densities, saturation, and fluid composition. No mass transfer is assumed between the liquid phase hydrocarbons and water. For numerical robustness, the governing equations are discretized using the adaptive-implicit method (Collins et al., 1992; Nghiem et al., 2004), which combines computational efficiency with solution stability.

Thermal effects are critical in these simulations due to the significant temperature differential between the injected CO_2 or water and the reservoir. This differential impacts the efficiency of heat extraction during the CPG stage. To model these effects, energy balance equations are incorporated to track the temperature distribution in the reservoir, accounting for convection, heat conduction, and heat losses to the surrounding rock layers (Vinsome and Westerveld, 1980). These energy equations are solved simultaneously with the mass and flow equations to ensure a comprehensive representation of reservoir dynamics.

Fluid modeling and phase behavior calculations were conducted using the WinProp simulator (Computer Modeling Group, 2024c), which generates detailed pressure–volume–temperature (PVT) models for compositional systems. Oil composition data were sourced from a large Middle Eastern oil field (Al-Mudhafar et al., 2022), and hydrocarbon components were grouped into representative pseudo-components to reduce model complexity. The original oil composition and pseudo-components, used in the simulations, as well as their calculated thermodynamic properties under initial reservoir conditions, are provided in Appendix A. CO_2 was modeled individually as it is the injection fluid for both CO_2-EOR and CPG processes.

Phase properties were described using the Peng–Robinson equation of state (Peng and Robinson, 1976) and viscosity was modeled using established correlations (Jossi et al., 1962; Yoonm and Thodos, 1970). Gas solubility in the aqueous phases was calculated using Henry's law with pressure–temperature adjustments (Harvey, 1996). Table 2 presents the oil phase properties under initial reservoir conditions, while Table A.4 summarizes additional key phase properties of the EOS-oil model, including API gravity, gas–oil ratio (GOR), minimum miscibility pressure (MMP), viscosity, and density.

Table 2
Oil phase properties under initial reservoir conditions.

Property	Value	Units
Gravity	40	API
GOR	44	m3/m3
MMP	175	bar
Viscosity	0.72	cp
Density	780	kg/m3

The density and viscosity of reservoir brine were calculated using the correlations of Rowe and Chou (1970) and Kestin et al. (1981), respectively, with salinity effects excluded. Additional details are available in the GEM User's Manual (Computer Modeling Group, 2024b) and WinProp documentation (Computer Modeling Group, 2024c).

Mineral trapping, other rock–fluid chemical interactions, and their geomechanical impacts (e.g., porosity and permeability changes) are not included in the models for either the CO_2-EOR or CPG stages, as they are beyond the primary focus of this study and were excluded for simplicity and consistency.

Relative permeability curves for water–oil and gas–liquid systems are provided in Appendix B. Oil relative permeability in the three-phase system was evaluated using a modified version of Stone's second model (Aziz and Settari, 1979). Capillary pressure and hysteresis effects were not considered.

2.3.2. Gridding

Structural gridding is applied to achieve spatial discretization of the computation domain, with each grid block measuring 10 x 10 x 1 m, resulting in a total of 125,000 cells (i.e., 50 grid blocks in all three directions). The grid size is chosen to be at least four times smaller than the smallest correlation length in each direction to ensure robust geostatistical permeability generation (see Section 2.1.1), as recommended by Räss et al. (2019) and Li et al. (2022).

2.3.3. Phase labeling

As addressed by several authors (Bennett and Schmidt, 2017; Hosseininoosheri et al., 2018; Sheth et al., 2023) accurate identification of phases under reservoir conditions is crucial for compositional numerical simulations involving CO_2 injection into oil reservoirs, especially when the densities of oil and supercritical CO_2 are similar. This similarity often occurs near the injection wellbore, where the cooler CO_2 has a relatively high density. By default, CMG-GEM utilizes a density-based phase labeling method (Computer Modeling Group, 2024b), which may result in inaccurate estimations of oil and CO_2 volumes in the reservoir. Therefore, in this study, we use a phase labeling method that determines phase identities based on supercritical conditions using the criteria presented by Gosset et al. (1986). Further details are given in the GEM User Manual (Computer Modeling Group, 2024b).

2.3.4. Well constraints

Simulations of waterflooding are conducted over a 10-year period at a constant injection rate of 0.1 pore volumes per year, calculated at the injector bottomhole conditions. Simulation results indicate that the water–oil ratio (WOR) exceeds 90% across all realizations, reaching approximately 95% in most cases by the end of 10 years. The 10-year mark is selected as the transition point to CO_2 injection, ensuring consistency across simulations by maintaining the same volume of injected water and thermal depletion due to cold water injection.

After waterflooding, CO_2 injection begins at a rate of 0.1 pore volumes per year. Due to the preferential flow of gas compared to

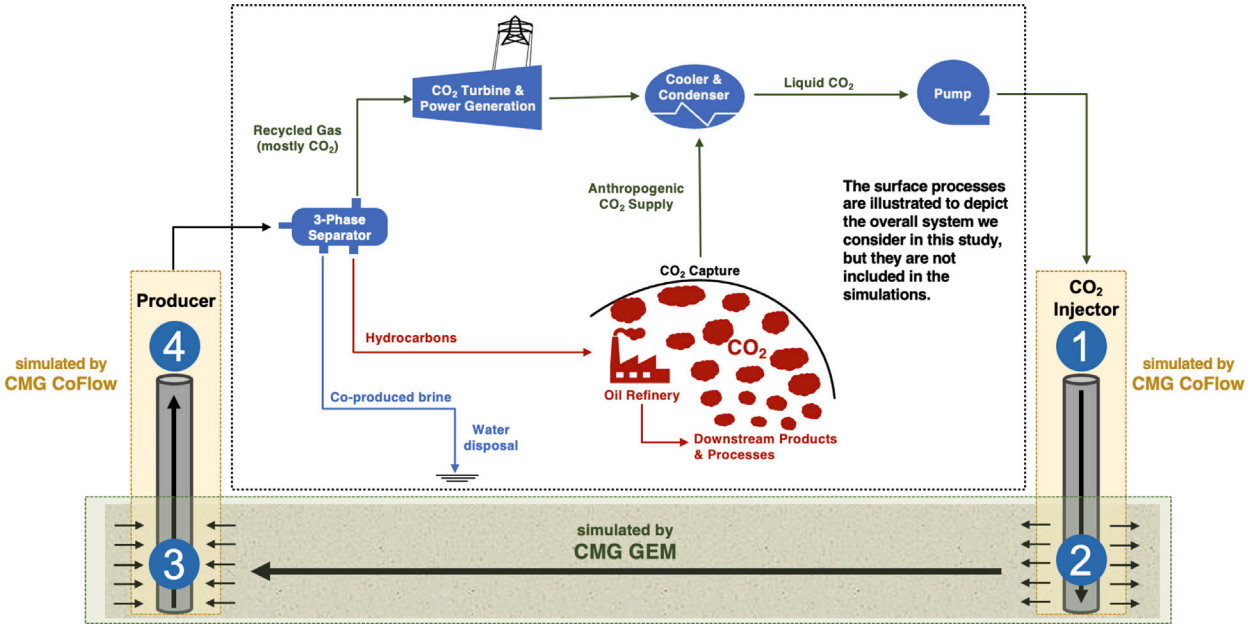

Fig. 3. Conceptual representation of a CPG system integrated with a CO_2-EOR operation. The boundaries of the simulated model and the simulation tools used are indicated. The processes occurring between Points 4 and 1 are illustrated to depict the overall considered system, however, they are not included in the simulations.

Table 3
Key parameters and constraints for well operations in the simulations.

Property	Value	Units
Water injection rate	0.1	pore volumes/year
Waterflooding duration	10	years
CO_2 injection rate (EOR)	0.1	pore volumes/year
CO_2-EOR duration	1	pore volumes
CO_2 injection rate (CPG)	0.5	pore volumes/year
CPG duration	10	pore volumes
Surface ambient temperature	15	°C
CO_2 injection bottomhole temperature	50	°C
Water injection bottomhole temperature	40	°C
Maximum bottomhole injection pressure	450	bar
Bottomhole pressure of producer	300	bar
Producer well radius	0.1	m
Injector well radius	0.2	m

liquids, CO_2 breakthrough occurs relatively early, leading to a gradual slowdown in incremental oil recovery. Once the incremental oil recovery plateaus and the gas-liquid ratio exceeds 90%, typically after 10 years, the transition from EOR to CPG is initiated (under Option d). At this stage, the CO_2 injection rate is increased to 0.5 pore volumes per year to enhance geothermal heat extraction. For comparison, this rate is approximately 2.5 times higher than the injection rate used during Phase 1 of the Northern Lights CCS Project (Thompson et al., 2022), and about 80% of the rate planned for Phase 2. In mass terms, the injection rates correspond to about 25 kg/s during EOR and 125–130 kg/s during CPG operations for the 1×1 km^2 inverted 5-spot well pattern model area.

It is important to note that the reported injection rates (see Table 3) do not directly reflect the amount of CO_2 permanently stored in the reservoir, as produced CO_2 is recycled into the injection stream. Details of the CO_2 sequestration aspect of the system are provided in Section 3.4.

The model boundaries considered in this study are shown in Fig. 3. The schematic illustrates the circulation of CO_2, starting from the injector wellhead (Point 1) to the injector bottomhole (Point 2), through the reservoir to the producer bottomhole (Point 3), and finally arriving at the producer wellhead (Point 4). Hydrocarbon and geothermal energy production rates are calculated and reported at Point 4 throughout the study. The well operating constraints applied in the simulations are summarized below:

1. *Injector wellhead:* The CO_2 injection temperature is set at 22 °C (Adams et al., 2015) with the injection fluid being pure CO_2 without impurities. The injection wellhead pressure is dynamically back-calculated throughout the simulation to maintain the required bottomhole pressure for the defined flow rate. This pressure evolves over time with changing reservoir conditions. During the CO_2-EOR stage, higher surface pressures are initially needed to displace reservoir fluids. As CO_2 saturation in the reservoir increases, the required surface pressure decreases. This reduction is further supported by the development of density-driven thermosiphon flow (Atrens et al., 2009; Adams et al., 2014, 2015).
2. *Injector bottomhole:* Based on correlations from the Standard Handbook of Petroleum and Natural Gas Engineering (Lyons et al., 2016), the subsurface rock fracturing pressure is estimated to be 450 bar at a depth of 3000 m, which we apply as the maximum bottomhole injection pressure constraint. The bottomhole injection temperatures for water and CO_2 are set to 40 °C and 50 °C, respectively.
3. *Producer bottomhole:* During waterflooding, the minimum bottomhole pressure is set at 20% below the hydrostatic reservoir pressure to enable oil production, simulating a combination of primary and secondary recovery methods (such as pump-assisted production and waterflooding). When CO_2-EOR begins, the initial (hydrostatic) reservoir pressure (~300 bar) is used as the minimum bottomhole pressure constraint. Reservoir conditions, including pressure, temperature, and fluid composition, as well as thermophysical properties of CO_2, oil, and water, are calculated by CMG-GEM as described previously.
4. *Producer tophole:* The bottomhole pressure and temperature of the produced fluid are transmitted to the surface via wellbore

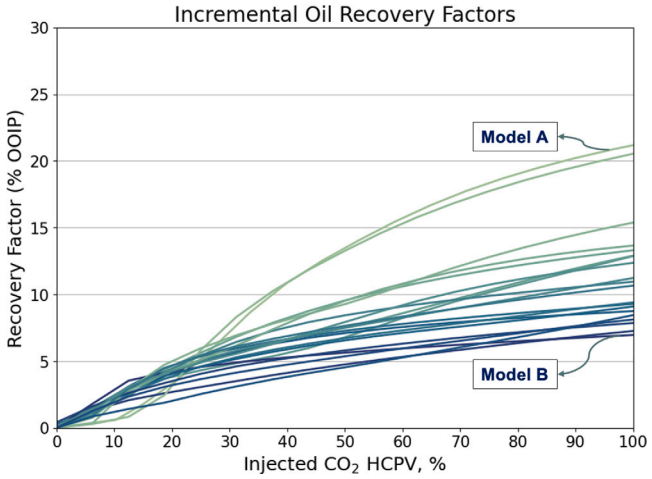

Fig. 4. Incremental oil recovery rates from CO_2-EOR simulations across 20 heterogeneous oil field realizations.

simulations using CoFlow (Computer Modeling Group, 2024a). Pressure changes along the wellbore are modeled using the Gray correlation (Gray, 1978). The thermodynamic properties of the supercritical CO_2 (e.g., specific enthalpy, density) at wellhead conditions are determined using the CoolProp library (Bell et al., 2014).

The wellbore model used to simulate transitions between Points 1 and 2 (injection) and Points 3 and 4 (production) is detailed in Appendix C.

3. Simulation results

This section presents the findings from the integrated modeling workflow, focusing on both CO_2-EOR and CO_2-Plume Geothermal stages. The results provide insights into the effectiveness of the combined CO_2-EOR–CPG system in maximizing resource utilization and enhancing overall energy recovery. Although we do not provide a full uncertainty quantification, the ensemble of 20 realizations is used to illustrate the variability in system performance.

The results are plotted against dimensionless time, t_D, which is defined in terms of the pore volume (PV) equivalent of injected fluid:

$$t_D = \frac{Qt}{\phi AL}, \tag{1}$$

where Q is the volumetric injection rate (m^3/day) calculated for the injector bottomhole conditions, t is time in days, ϕ is rock porosity, and A (m^2) and L (m) are the reservoir's area and length, respectively. However, oil recovery rates are typically presented relative to the hydrocarbon pore volume (HCPV), where HCPV = $t_D S_{oi}$ and S_{oi} is the initial oil saturation in the reservoir.

3.1. Comparing simulation results with published CO_2 -EOR field data

As shown in Fig. 4, the heterogeneous reservoir realizations yield incremental oil recovery values ranging from approximately 7% to 21% of the original oil in place (OOIP), with the majority of models demonstrating an incremental recovery factor below 15%. These values closely align with actual field data (Azzolina et al., 2015; Lake et al., 2018, 2019; Farajzadeh et al., 2020). The figure also illustrates that incremental oil recovery increases sharply shortly after the initiation of CO_2 injection, particularly before 0.1 HCPV. However, in some cases, especially in those with higher ultimate recovery, it takes longer to observe significant oil recovery. In these cases, the CO_2 plume contacts a larger pore volume, displacing more oil toward the production wells and resulting in higher overall oil recovery.

In Fig. 4, the simulation results are color-coded, according to their respective EOR performance, ranging from blue (low incremental oil recovery) to green (high incremental oil recovery). The two extreme cases, Model A, with the highest recovery factor, and Model B, with the lowest, are highlighted to illustrate the range of performance. These models will be referenced throughout the remainder of the study, with this color-coding scheme applied consistently to facilitate comparisons.

3.2. Phase mass flow rates and bottomhole temperature at the producer

While the incremental oil recovery rate is a key performance parameter during EOR, reservoir heterogeneity influences many other aspects of CO_2 injection operations. One significant outcome of this heterogeneity is the dynamic and distinct evolution of the CO_2-plume within the reservoir both temporally and spatially, significantly influencing fractional phase production rates, heat depletion within the reservoir, and changes in fluid temperature at the producer, all critical parameters for the CPG stage.

Fig. 5 illustrates the fractional mass flow rates of oil, water, and gas (here, the gas phase refers to supercritical CO_2 and any produced hydrocarbon gases) at various simulation stages (i.e., waterflooding, CO_2-EOR, and CPG) for two distinct models: Model A and Model B. The x-axis represents fluid injection in terms of pore volumes, with initial water injection followed by CO_2 injection for EOR, both at a rate of 0.1 PV/year, for a total of 1 pore volume injected for each fluid. During waterflooding, the water fraction (also known as water cut) in the produced fluid increases to approximately 90%–95% in all models before CO_2 injection begins. During the EOR stage, Model B, characterized by lower incremental oil recovery, experiences early CO_2 breakthrough, resulting in a steep increase in CO_2 mass fraction and minimal oil recovery, as CO_2 preferentially channels through high-permeability zones more readily than water, exacerbating conformance issues. In contrast, Model A demonstrates a more gradual increase in CO_2 mass fraction and significantly higher oil recovery, as its CO_2 plume contacts a larger volume of oil-saturated rock. The behavior in other models follows similar trends based on their heterogeneity.

This behavior is further visualized in Fig. 6, which tracks the CO_2 saturation in Models A and B during the EOR and CPG phases. Model A achieves a broader sweep of the reservoir by the end of the EOR stage, whereas Model B, with its early breakthrough, exhibits limited CO_2 plume development. As CO_2 injection continues during the CPG phase, the CO_2 plume in both models extends into previously unswept regions, further improving the ultimate sweep efficiency in both models.

A common observation from the simulations is the high mobility of CO_2 under reservoir conditions leading to predominantly CO_2 flow in the producer. By the end of the CO_2-EOR stage, the gas fraction in the produced fluid reaches around 90% in nearly all models. Upon transitioning to the CPG stage, with the CO_2 injection rate increased to 0.5 PV/year, the gas mass fraction exceeds 95%, while co-produced water and oil volumes vary in each model. Produced gas predominantly consists of CO_2, as shown in Fig. 7, with minimal hydrocarbon gas production.

Fig. 8 depicts the evolution of fluid temperature under the bottomhole conditions of the production well during all stages. During waterflooding, up to 12 °C cooling is observed in some models, such as Model B, due to early water breakthrough. In contrast, other models (e.g., Model A) exhibit no significant cooling at the producer during this stage. However, cooling occurs around the injector and in permeable zones, where water flows preferentially.

During the EOR stage, injected CO_2 displaces oil and water through both water-swept and previously bypassed sections of the reservoir. As CO_2 injection continues into the CPG stage, reservoir heat depletion becomes more significant. Some models show moderate temperature

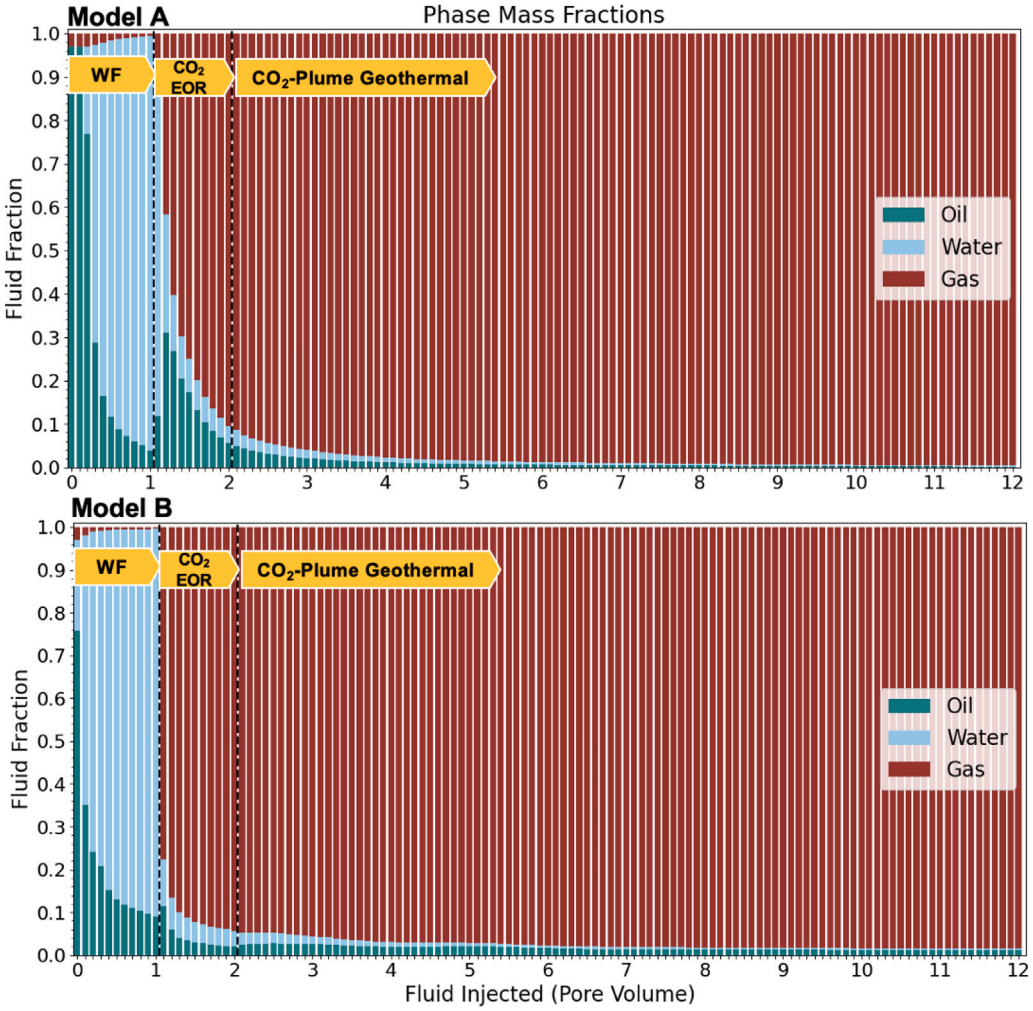

Fig. 5. Fractional mass flow rates at the production well under surface conditions. (a) Model A: Better sweep efficiency and higher incremental oil recovery, (b) Model B: Poor sweep efficiency and lower incremental oil recovery. Each bar represents 0.1 PV fluid injection, equivalent to 1 year during waterflooding and CO_2-EOR. As the injection rate is increased to 0.5 PV/year in CPG stage, each bar represents 0.2 years at that stage.

declines (around 10 °C), while others experience more pronounced cooling (up to 50 °C), reducing fluid temperature from 120 °C to approximately 70 °C by the end of the CPG operations. The color-coding from Fig. 4 is maintained here to differentiate models by their incremental oil recovery factors, but no clear correlation is observed between EOR performance and thermal breakthrough at the producer.

3.3. Energy analysis: comparing energy production during EOR and CPG stages

The thermal power output of the CPG system, expressed in kilowatts (kW), is calculated as

$$Q_{\text{thermal}} = \dot{m}_{CO_2} \cdot \Delta h_{CO_2}, \tag{2}$$

where, $\dot{m}_{CO2}$ is the mass flow rate of CO_2 at the production well (kg/s), and Δh_{CO_2} represents the specific enthalpy difference between the produced and injected CO_2 (kJ/kg). The enthalpy difference is computed using CoolProp (Bell et al., 2014) based on wellhead pressure and temperature conditions. It is important to note that this calculation represents the gross energy extracted, without accounting for system inefficiencies.

The thermal power outputs calculated during the CPG stage are shown in Fig. 9. In most models, thermal power output rapidly peaks within the range of 13–23 MW, while a few models achieve this after approximately 2 pore volumes (PV) of CO_2 injection at a rate of 0.5 PV/year. By the end of 10 PV of CO_2 injection, the decline in power output from the peak ranges from about 6% to slightly more than 40% across all subsurface realizations, with an average decline of 24%.

The color-coded lines show no observable correlation between incremental oil recovery during the EOR stage and the thermal power output of the integrated CPG system, which is consistent with the lack of correlation observed in production temperatures. For example, Model A, represented by a dashed green line in Fig. 9, achieves the highest oil recovery factor after the EOR stage but performs below average in thermal power output during the CPG stage. Conversely, the model with the highest CPG thermal power output is represented by a darkish blue color, indicating that its EOR performance ranks among the lowest of all heterogeneous models simulated in this study.

To evaluate the significance of the thermal energy production from the CPG operation, we can compare CPG's thermal energy production with the gross chemical energy of the oil produced during EOR. The lower heating value (LHV) of crude oil can be assumed to be the chemical energy contained in compositionally complex crude oils, or in other words, the amount of heat released during its combustion. The equation relating the LHV of oil to its specific gravity (SG) is

$$LHV\left[\frac{\text{MJ}}{\text{kg}}\right] = 55.5 - 14.4 * SG. \tag{3}$$

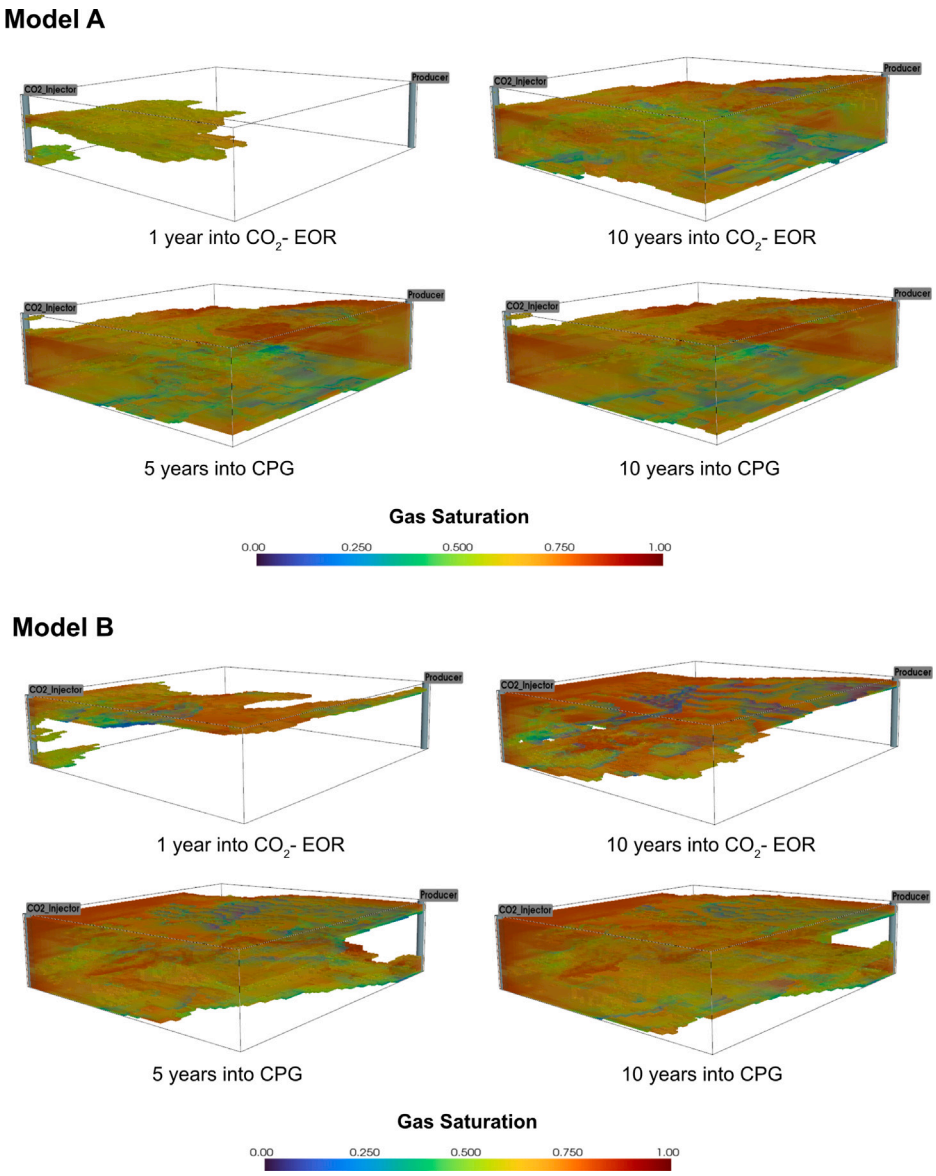

Fig. 6. Spatial and temporal evolution of the CO_2 plume in two example models. Model A exhibits relatively good sweep efficiency, while Model B shows limited sweep efficiency. Regions with CO_2 saturation below 5% are excluded from visualization.

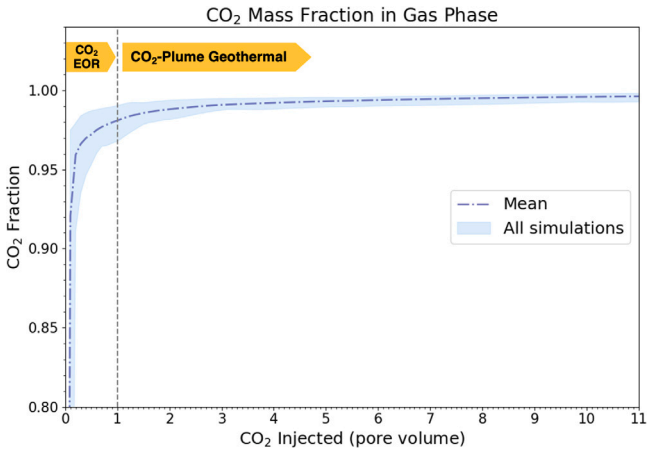

Fig. 7. CO_2 mass fraction in the produced gas.

Assuming a specific gravity (SG) of 0.80, the lower heating value (LHV) of crude oil is approximately 44 MJ/kg. By multiplying the oil mass flow rates from GEM by the LHV, we calculate the total chemical energy produced during the EOR stage in megajoules (MJ). Similarly, the thermal power generated during the CPG stage is used to compute the total thermal energy output in MJ.

Fig. 10 compares the total gross energy production from EOR and CPG. The thermal energy extracted during CPG (shown as hatched bars) ranges from 0.85×10^{10} MJ to 1.5×10^{10} MJ, with an average of 1.2×10^{10} MJ. In contrast, the chemical energy from oil during EOR spans a wider range, from 2.2×10^{10} MJ to 6.5×10^{10} MJ, with an average of 3.7×10^{10} MJ.

The percentages next to the bars represent the additional energy contribution of CPG relative to EOR. For example, in Model A, CPG contributes an additional ~20% of the energy produced during EOR, while in Model B, it contributes an additional 42%. Models with higher oil recovery factors tend to yield smaller proportional gains from CPG, and vice versa; however, no consistent pattern emerges when comparing CPG and EOR energy outputs across all models.

This comparison underscores that integrating CPG with EOR can enhance total energy recovery by approximately 20% to 50%.

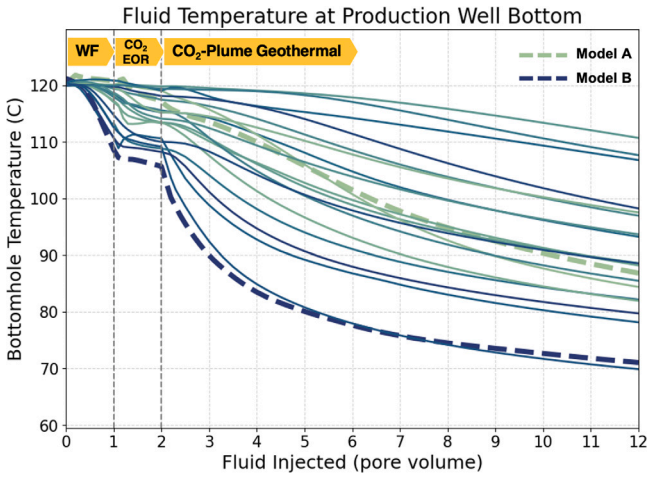

Fig. 8. Bottomhole temperature of the production fluid for the different stages of the simulations.

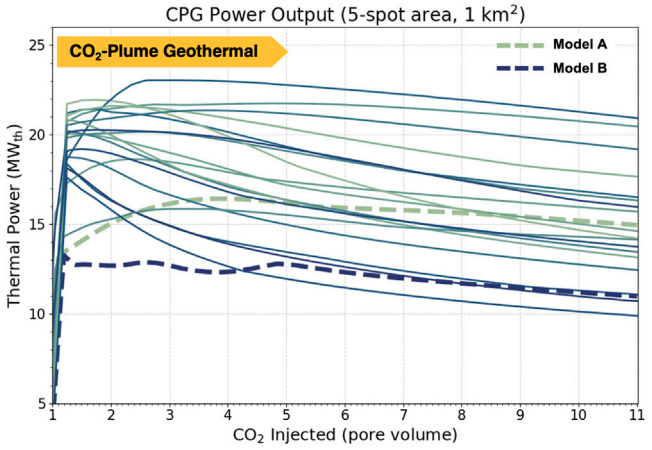

Fig. 9. CPG-generated thermal power production rates per reservoir footprint area of the 1 km^2 5-spot inverted well pattern. Shown results are for the heterogeneous models during the CPG stage.

3.4. Carbon sequestration

As illustrated in Fig. 3, the injected fluid consists of geothermally heated and recycled CO_2—CO_2 that has been produced from the reservoir, separated, processed through thermal power generation units, and condensed into a liquid phase, and typically combined with new (basically make-up) CO_2 coming from a CO_2 capture unit. While the CO_2 injection rate remains constant during EOR and CPG operations (see Section 2.3.4), the ratio of recycled to make-up CO_2 varies over time due to the increasing rate of CO_2 production (see Fig. 5).

To estimate the amount of CO_2 sequestered during both the EOR and CPG stages, we consider only the make-up CO_2 added to the system. This is determined by subtracting the cumulative produced (recycled) CO_2 from the total injected CO_2, excluding potential surface losses and leakages. Fig. 11 presents the mass of CO_2 sequestered (in million tons) during EOR and CPG operations. In the 1 km^2 simulated area, approximately 1 to 3 million tons of CO_2 are stored geologically during the EOR stage. The subsequent CPG phase increases this by 80% to 280%. The bars in the figure represent total CO_2 mass sequestration, which includes structurally trapped CO_2 and CO_2 dissolved in reservoir water (i.e., dissolution trapping). Residual trapping is excluded from the analysis as the effect of hysteresis is neglected.

As mentioned, integrating CPG with EOR extends CO_2 injection, prolonging the operational life of the field. This continued CO_2 injection during the CPG stage allows the CO_2 plume to grow further, sweeping areas of the reservoir that were previously bypassed. This study represents one of the first attempts to simulate CO_2 circulation, including both injection and production, within oil fields, extending the project beyond the conventional economic limits of typical EOR projects. In this analysis, we estimate and present the changes in gas saturation across both operational stages (Fig. 12).

The rate of growth (ROG) of the CO_2 plume is determined by comparing the average CO_2 saturation in the reservoir pore space before and after the CPG stage. In Fig. 12, the green lines illustrate the CO_2 saturation in each of the 50 layers of the model (each layer representing a 1-meter-thick horizontal section) following the EOR phase. The yellow line represents the saturation after the CPG stage. The ROG is calculated by dividing the total average CO_2 saturation after the CPG stage by the average CO_2 saturation at the end of the EOR stage.

Our analysis shows that the ROG of the CO_2 plume varies from 47% in the lowest case to 271% in the highest case, with an average of approximately 120%. This indicates substantial growth of the CO_2 plume during the CPG stage, which increases the total volume of swept reservoir and, consequently, the amount of CO_2 sequestered.

Integrating CPG into a reservoir after CO_2-EOR enhances CO_2 sequestration through both structural trapping and thermodynamic effects. As the reservoir cools, CO_2 density increases, enabling greater mass storage per unit volume. Additionally, the back-production of CO_2 helps mitigate pore-fluid pressure buildup, allowing for sustained injection at higher rates and improved heat extraction from the rock (Hau et al., 2025).

Fig. 11 quantifies the additional CO_2 storage driven by density changes in the CO_2 plume region post-EOR, represented by the orange bars. These temperature-induced effects increase total CO_2 sequestration by 9%–20% compared to EOR alone, extending the benefits of initial CO_2 storage and reinforcing the viability of CPG as a long-term sequestration strategy. For completeness, the thermodynamic effects of reservoir cooling on CO_2 density are further examined in Appendix E, where plume density evolution is shown on a pressure–temperature diagram for the two example models (Fig. E.19).

3.5. CO_2 utilization

The *CO_2 utilization factor* (Eq. (4)) is a critical parameter that reflects the efficiency of CO_2 injection in generating value. In CO_2-EOR operations, this parameter quantifies the incremental oil produced per unit of CO_2 injected, whereas, in the context of CPG, it represents the geothermal power generated per unit of CO_2 injected. However, since the produced CO_2 is recycled and reinjected in both CO_2-EOR and CPG operations, relying solely on injected CO_2 can be misleading when evaluating the overall effectiveness. We thus employ the *net CO_2 utilization factor* (Eq. (5)) which offers a more accurate assessment as it compares the value generated to the amount of CO_2 permanently sequestered in the reservoir.

$$\text{CO}_2\text{ Utilization Factor} = \frac{\text{Value generated by EOR or CPG}}{\text{CO}_2\text{ Injected}} \tag{4}$$

$$\text{Net CO}_2\text{ Utilization Factor} = \frac{\text{Value generated by EOR or CPG}}{\text{CO}_2\text{ Injected} - \text{CO}_2\text{ recycled}} \tag{5}$$

The energy generated from EOR and CPG operations can be evaluated using a common metric, expressed in megajoules (MJ) of energy produced per ton of CO_2 sequestered. The top plot in Fig. 13 demonstrates how integrating CPG with EOR improves the net CO_2 utilization factor. At the end of the EOR stage, this ratio ranges from 17 to 26 GJ/ton CO_2 across all models. Following the CPG operation, the range

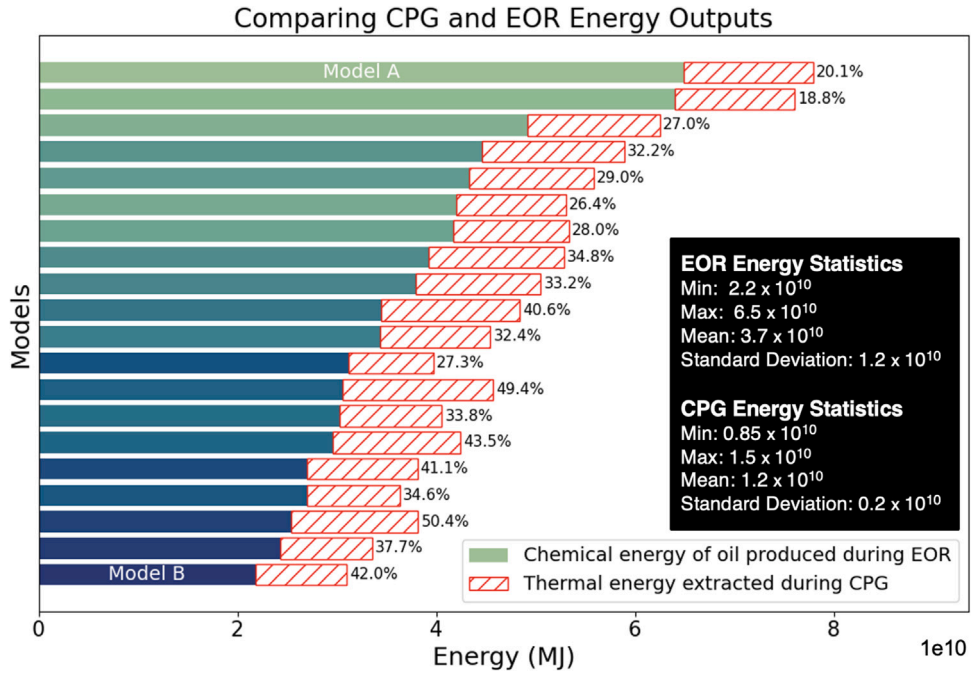

Fig. 10. Comparison of total low heating value (LHV) of oil produced during EOR and thermal energy extracted during CPG from the heterogeneous models. The percentages next to the bars show the ratio of cumulative thermal energy production from CPG operation to the total chemical energy of the EOR oil.

shifts upwards to 21–31 GJ/ton CO_2 sequestered. The enhancement in net CO_2 utilization varies between 2.7 and 8.5 GJ/ton CO_2 across the models, representing an increase of approximately 13%–37%. This improvement highlights the potential of CPG to significantly enhance energy recovery and CO_2 utilization efficiency when integrated with EOR.

The smaller plots in the figure provide further insights into the components of the net CO_2 utilization factor for EOR and CPG. The lower-left plot shows the net CO_2 utilization factor for EOR, expressed in stock tank barrels (STB) of oil per ton of CO_2 sequestered. Our simulations reveal that oil recovery stabilizes toward the end of the EOR stage, with most models achieving 2.5–3.5 STB per ton of CO_2. The lower-right plot presents the net CO_2 utilization factor for CPG, expressed in megawatt-hours (MWh) of geothermal power per ton of CO_2 sequestered. During the CPG stage, geothermal power production varies more widely across models, ranging from approximately 700 to 2400 kWh per ton of CO_2 sequestered. By combining these metrics, the analysis shows that for every barrel of oil produced during EOR, the integration of CPG can generate an additional 330–980 kWh of thermal power.

4. Discussion

4.1. Incremental oil recovery rates during CO_2-EOR

The representativeness of the conceptual models is validated by demonstrating that the oil recovery and CO_2 utilization factors from our simulations closely align with actual field observations (Azzolina et al., 2015; Lake et al., 2018, 2019; Farajzadeh et al., 2020). Following an initial rapid increase, the rate of oil recovery gradually stabilizes as CO_2 injection progresses and CO_2 breakthrough occurs at the production well. This trend, captured in our synthetic reservoir simulations, highlights the ability of the models to address a common challenge in CO_2-EOR: CO_2 channeling through high-permeability zones, leaving extensive unswept regions. Such conformance issues, driven by the high mobility of CO_2 and often large reservoir heterogeneities, are well-known in the EOR literature (Hamouda and Bagalkot, 2019; Massarweh and Abushaikha, 2022).

Importantly, our models are not designed to replicate a specific field case or precisely match the recovery factors presented in the reference studies. Instead, the goal of this comparison is to ensure that the recovery factors obtained from our simulations fall within a reasonable range when compared to actual field examples and that they are consistent with observed results.

4.2. CO_2-plume dynamics and sweep efficiency

Our simulations reveal distinct CO_2 plume behaviors across the models, driven by reservoir heterogeneity. In some models, the CO_2 plume forms a thin layer between the injector and the producer, bypassing significant rock volumes. In others, CO_2 sweeps through larger permeable sections, resulting in higher oil recovery. Fig. 6 illustrates this variability in CO_2 plume behavior with two representative models.

These differences in CO_2 plume behavior significantly impact oil recovery rates, gas breakthrough times, and dynamic phase flow changes, such as increasing gas-oil ratios over time, as shown in Figs. 4 and 5. These findings are consistent with actual field observations, exhibiting irregular CO_2 plume flow behavior, validating the accuracy of our synthetic model simulations (Ampomah et al., 2017; Williams and Chadwick, 2017, 2021; Nazarian et al., 2022; Hau et al., 2025).

Fig. 5 shows that the produced fluid mass fraction is predominantly supercritical CO_2 at the start of the CPG stage, in contrast to greenfield CPG systems that require a plume-establishment period before sufficient CO_2 saturation reaches at the production well (Ezekiel et al., 2020), enabling immediate and efficient geothermal energy extraction.

During the CPG stage, continued CO_2 injection results in the CO_2 plume to grow and sweep previously bypassed regions of the reservoir. Our study is among the first to simulate CO_2 circulation, combining CO_2 injection and production, in oil fields, extending beyond the economic limit of EOR, offering insights into the CO_2 saturation evolution over time (Figs. 6 and 12).

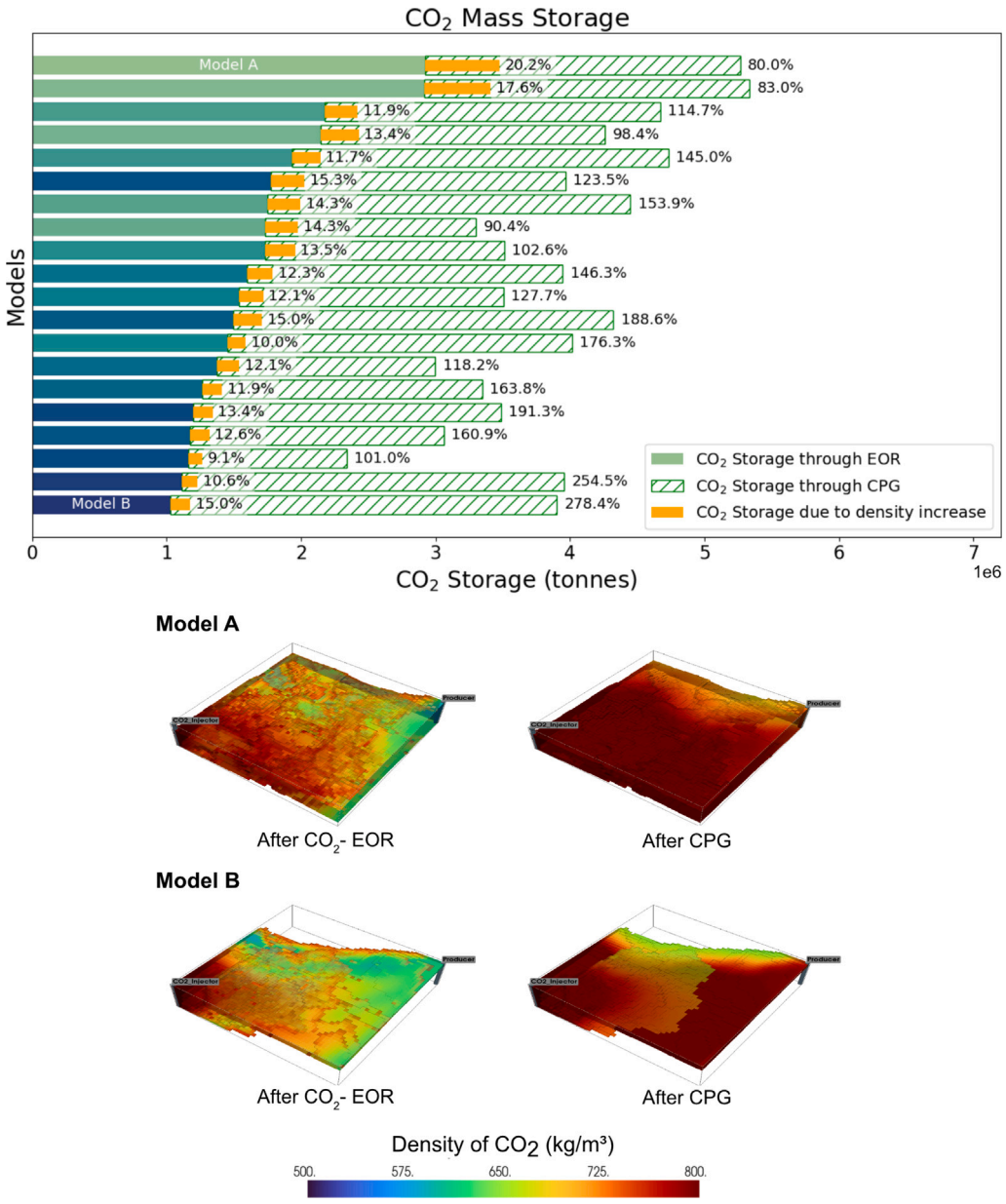

Fig. 11. CO_2 storage across different operational stages. Solid bars show storage during the EOR stage, and dashed bars show storage during the CPG stage. Orange bars indicate additional CO_2-stored during CPG due to density increase in previously swept regions, caused by reservoir cooling, pressure changes, plume migration, and compositional effects. The lower panel illustrates the change in average density of the supercritical CO_2 plume between the end of the EOR and CPG stages.

In Fig. 12, the green lines represent an uneven displacement front, caused by CO_2 channeling through high-permeability layers. As CO_2 injection continues into the CPG stage (yellow lines), the displacement front becomes more uniform due to the merging of CO_2 plume "branches", driven by horizontal and vertical cross flow. This behavior reflects permeability interconnectivity and layer communication, as described by Khan and Mandal (2021).

It is important to note that the entire 50-meter vertical section of the reservoir is perforated at the injection wellbore, with flow apportionment among the perforations determined by the GEM simulator under a maximum CO_2 injection bottomhole pressure constraint (detailed in Section 2.3.4). As the CO_2 saturation increases in some layers, the pressure gradient, required to circulate CO_2 in those layers, decreases, redirecting flow to previously unswept or low-CO_2-saturation regions. This redistribution promotes the merging of CO_2 plume branches described above. While the described CO_2 injection design is consistently applied in all models, actual field operations typically optimize the well perforation design based on reservoir conditions.

4.3. Evaluating the impact of CPG integration after CO_2-EOR

While it may be intuitive to assume that high EOR performance would correlate with strong CPG performance, as both benefit from effective CO_2 sweeps, the dynamics of CO_2 plume migration complicates this relationship. The color-coded thermal rates in Fig. 9 illustrate that incremental oil recovery and geothermal energy extraction do not always align. For instance, Model A, represented by a green dashed line in Fig. 9, achieves the highest oil recovery after EOR but performs

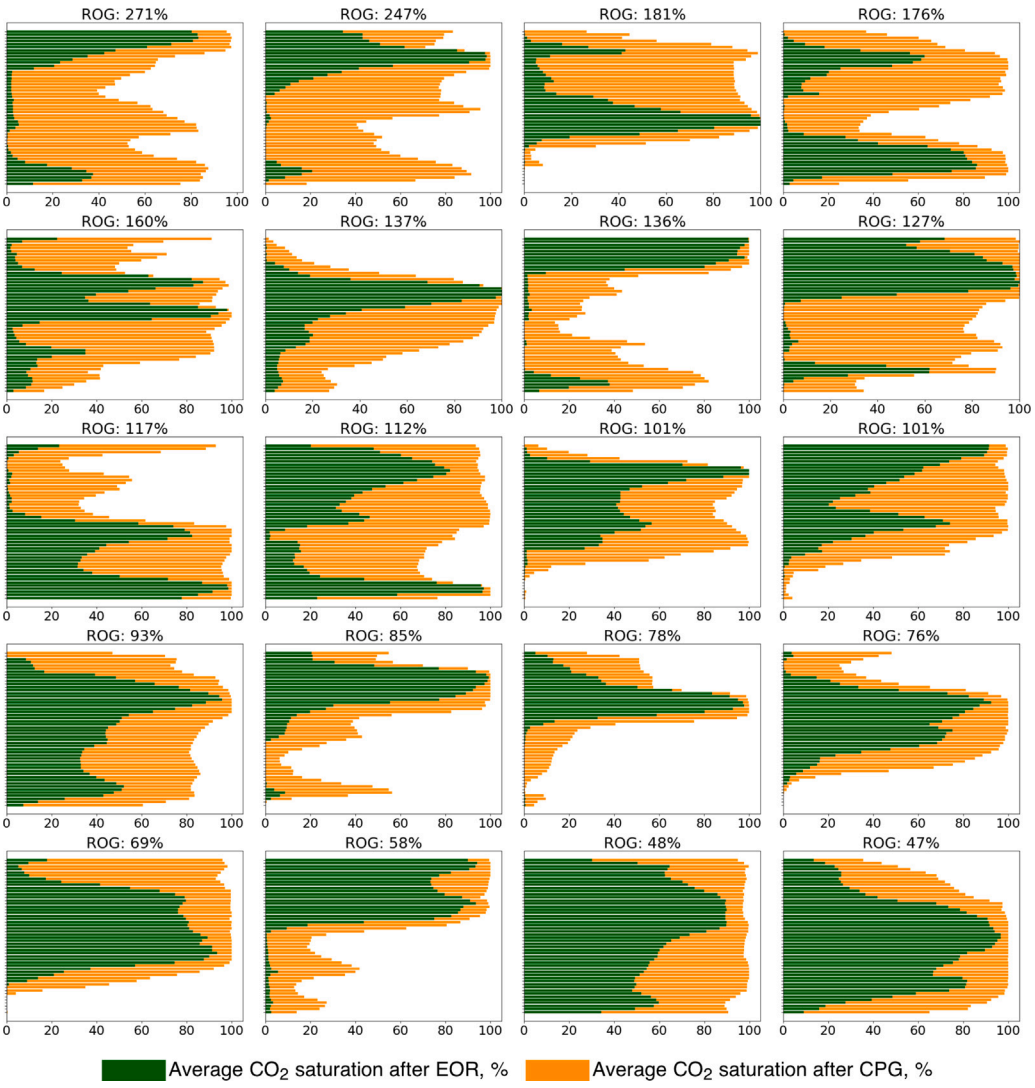

Fig. 12. Visualization of the average pore-space CO_2 saturation in each reservoir layer, shown in green and yellow for the CO_2-EOR and the CPG stages, respectively, at the end of the operations for all models. Each bar on the vertical axis represents 1 meter reservoir thickness, with a total thickness of 50 m. The CO_2 plume includes regions, where the pore-space CO_2 saturation exceeds the critical threshold of 5%.

below average among models during CPG. In contrast, the model that achieves the highest CPG thermal power output is shown in dark blue, signifying that its EOR performance is among the lowest of all heterogeneous models analyzed in this study.

Bottomhole fluid temperature trends (Fig. 8) further illustrate this lack of correlation across the stages of the EOR-CPG integrated system. During waterflooding, for example, Model A experiences minimal cooling as the injected, cold water sweeps through a larger rock volume, whereas Model B undergoes rapid cooling due to the limited water-sweep volume. However, when CO_2 injection for EOR begins, this trend reverses: Model A cools more rapidly, whereas the cooling in Model B slows and stabilizes. In some cases, even a slight temperature increase is observed, when CO_2-EOR commences. As CO_2 injection progresses into the CPG stage, the bottomhole temperatures continue to vary, based on the CO_2 plume flow characteristics, which are in turn determined by the heterogeneity of the geologic reservoir models.

The bottomhole temperature trends can be attributed to several factors:

1. CO_2 sweeping through previously water-swept rock can reduce the rate of cooling or even cause slight heating, as the bottomhole injection temperature of CO_2 is higher than that of water. Additionally, CO_2 has a lower heat capacity than water, leading to more gradual cooling.
2. In some cases, the CO_2 plume pushes previously injected cold water toward the production well, causing a sudden temperature drop at the bottom of the well.
3. In several simulations, CO_2 channels through relatively thin reservoir sections, cooling these regions, while the bulk of the rock retains higher temperatures, supplying heat via conduction, even though heat conduction is slow and thus has a limited impact.
4. The propagation of the CO_2 plume into thus far unswept (and still hot) reservoir sections helps maintain higher CO_2 temperatures at the production well bottom.

As detailed earlier and illustrated in Fig. 12, the CO_2 saturation profile and the CO_2 distribution shift considerably throughout CPG operations, compared to the conditions at the end of EOR, supporting the above-discussed trends. These variations in thermal and fluid

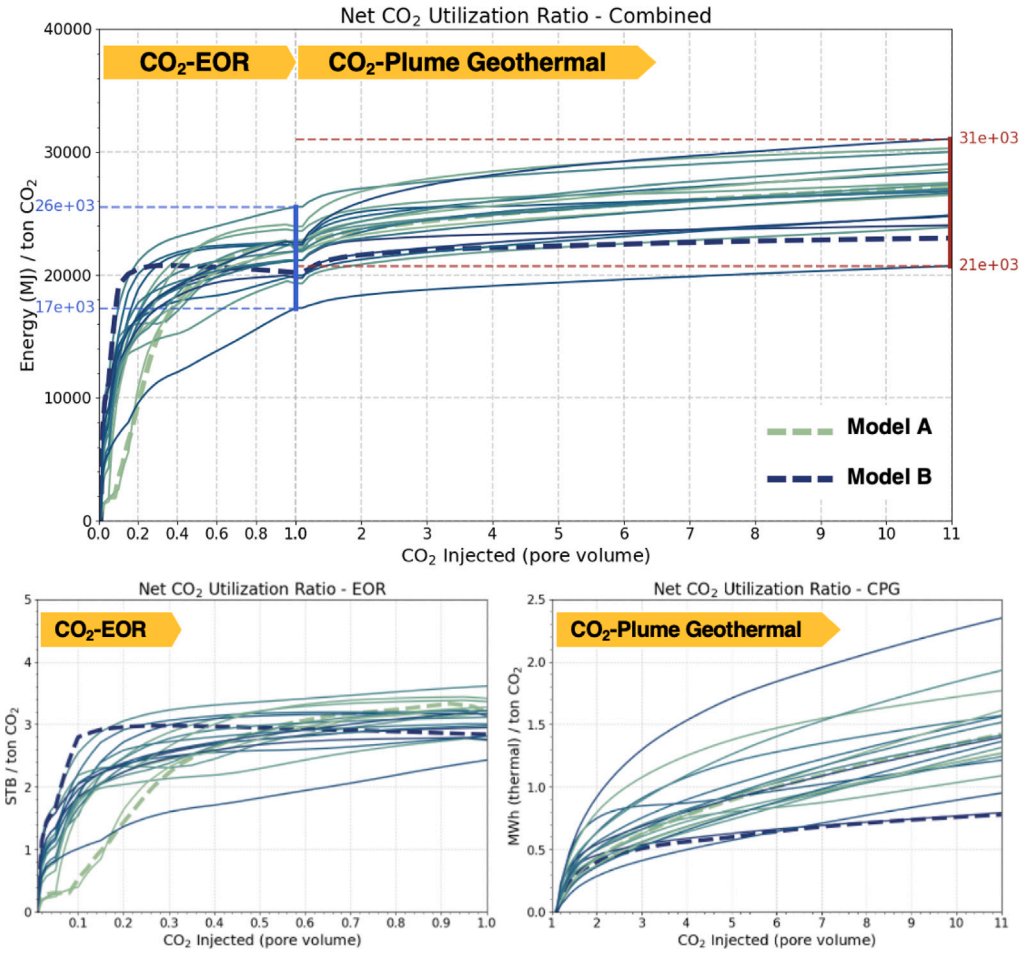

Fig. 13. Net CO_2 utilization factors during EOR and CPG operations. The top plot shows the combined net CO_2 utilization factor (in megajoules (MJ) per ton of CO_2 sequestered), illustrating the enhancement achieved by integrating CPG with EOR. For better visualization, the EOR portion of the top figure has been magnified laterally by a factor of three. The lower-left and lower-right plots detail the individual contributions from EOR and CPG, expressed as incremental oil recovery (in STB/ton CO_2) and geothermal energy generation (in MWh/ton CO_2 sequestered), respectively.

flow dynamics indicate that CPG performance is influenced by the CO_2 plume migration characteristics, occurring after EOR, making it difficult to predict CPG performance solely based on EOR results.

4.3.1. Energy analysis

Across the 20 conceptual oil fields simulated in this study, the thermal power output from CPG, following CO_2-EOR, ranges from 13 to 23 MW_{th}/km^2, based on a single 1 km^2 inverted five-spot well pattern footprint and the design parameters described in Section 2.3. This demonstrates that integrating CPG with EOR at a full-field scale has the potential to deliver significant clean energy, while extending the productive lifespan of oil fields.

Fig. 10 compares the chemical energy from EOR, measured as the heat released during oil combustion, with the thermal energy delivered by the CPG operation. During the EOR stage, total chemical energy production varies widely across the 20 models, ranging from 2.2×10^{10} MJ to 6.5×10^{10} MJ, a threefold difference between the highest and lowest performers. In contrast, the CPG stage exhibits a narrower range of variability, with total thermal energy production differing by a factor of 1.75 across models.

These results suggest that reservoir heterogeneity has a more pronounced impact on CO_2-EOR performance, compared to CPG performance, at least under the current operational settings, such as CO_2 injection rate, bottomhole pressures, and injection temperature. This difference can be attributed to the gradual stabilization of CO_2 plume branches as CO_2 injection continues at higher rates during CPG than during EOR, as discussed in Section 4.2. Additionally, the displacement of original fluids (brine and oil) during EOR is strongly influenced by the heterogeneity of the rock permeability, whereas CPG benefits from being operated in a reservoir that already contains CO_2, reducing the effects of reservoir heterogeneity during geothermal energy production. Finally, heat transfer also occurs through the solid rock matrix of the reservoir by heat conduction, albeit slowly, compared to heat advection, whereas fluid mass (water, oil, CO_2) movement can only occur through the pore space. Consequently, fluid mass movement is more strongly affected than conductive heat transport by the reservoir's pore space permeability and, hence, the heterogeneity of the permeability field. This effect is more pronounced when overall reservoir permeabilities are lower, as heat advection to heat conduction ratios are lower (i.e., lower Peclet numbers prevail), or in other words, heat conduction plays a somewhat more significant role, amplifying the above effect slightly.

An intriguing observation is that thermal power outputs during CPG operations exhibit only a gradual decline (Fig. 9), even as bottomhole temperatures show a more pronounced drop (Fig. 8). This effect is caused by the increased density of CO_2 at the production well inlet (i.e. at reservoir depth), as the reservoir cools, raising the wellbore fluid pressure, so that, under constant bottomhole pressure constraints, the

wellhead pressure is reduced, thereby slowing the decline in the CO_2's specific enthalpy at the wellhead. Since the CO_2 injection enthalpy at the injector wellhead remains constant, the surface enthalpy difference (Eq. (2)) decreases more gradually than the bottomhole temperature, contributing to the relative stability of thermal power output.

Furthermore, in some models, the CO_2 mass production rate increases over time, approaching the CO_2 injection rate (Appendix D). This compensates for the decline in the specific enthalpy of the produced CO_2, further supporting a sustained thermal power output during CPG operations.

Maximizing the geothermal energy output of CPG operations could involve incorporating layers beyond the oil pay zone, such as residual oil zones (ROZs) or underlying aquifers. Previous studies by Koperna et al. (2006), Honarpour et al. (2010), and Ren and Duncan (2019) explored CO_2 injection in ROZs, primarily focusing on EOR and CO_2 sequestration. Expanding the usable volume of the reservoir to include ROZs and brine aquifers could significantly enhance CO_2-based geothermal energy production, a promising subject for future research.

It is also worth noting that the lifespan of CPG operations is not constrained by the time frame analyzed in this study. CPG can continue until heat depletion reaches threshold levels that render geothermal operations technically and/or economically unfeasible. The reported values are specific to the system and time frame considered here, ensuring consistency across all models. However, significantly higher thermal power production may be achievable with extended CPG operations beyond the scenarios presented.

In this study, we report gross energy outputs for both CPG (thermal) and EOR (chemical) in order to provide a consistent comparison. Conversion to electricity or other useful work would require additional, application-specific efficiency assumptions, which are beyond the scope of this work.

Future research should further explore the optimal balance between CO_2 injection rates and their impact on energy production for both EOR and CPG, as this could provide valuable insights into maximizing the efficiency and performance of integrated CO_2 utilization systems. In parallel, while this study does not directly address economics, previous work has examined cost ranges for CPG systems (Schifflechner et al., 2024; Rangel-Jurado et al., 2022), and CO_2-EOR cost analyses are widely available in the literature. A dedicated assessment of the transition costs from EOR to CPG will therefore be an important avenue for future research.

4.3.2. Enhanced CO_2 sequestration and CO_2 utilization factors

This study highlights how continued CO_2 injection during the CPG stage following EOR enhances total structural CO_2 sequestration by sweeping previously bypassed regions of the reservoir (see Section 4.2). Fig. 11 quantifies this effect across all models, demonstrating that integrating CPG with CO_2-EOR significantly increases the ultimate CO_2 storage potential, with the results being affected by the reservoir heterogeneity. Additionally, heat depletion during CPG operations contribute uniquely to the CO_2 sequestration potential: As the reservoir cools during CPG operations, the in-situ CO_2 density increases, enabling a greater mass of CO_2 to be stored per unit volume of pore space (confirming the findings of Hau et al. (2025)). This incremental effect is illustrated in Fig. 11 by the orange bars. Furthermore, the back-production of CO_2 reduces pressure buildup, enabling higher CO_2 injection rates and sustained heat extraction during the CPG stage, which further increases the density and storage capacity of supercritical CO_2 in the reservoir.

Another important observation from the simulations is that the CO_2 sequestration performance across the models generally correlates with its EOR success; models with higher oil recovery typically achieve greater CO_2 sequestration due to the improved volumetric sweep efficiency. However, additional sequestration during CPG, driven by structural CO_2 trapping and density-based CO_2 storage, does not directly correlate with the initial CO_2 sequestration performance due to the evolving spatial and temporal dynamics of the CO_2 plume. This underscores the necessity of site-specific, detailed reservoir modeling and integrated EOR-CPG simulations across all operational stages to more accurately estimate the final CO_2 sequestration potential of an oil field after EOR.

A critical consideration is that additional CO_2 injection can continue after EOR for dedicated CO_2 sequestration. Although our study does not directly compare post-EOR CPG with standalone CO_2 sequestration, CPG offers unique advantages in that regard. By circulating CO_2 through production wells, CPG reduces the reservoir pore-fluid pressure, enabling sustained injection rates while mitigating caprock fracturing risks, which might arise in purely CO_2 sequestration-focused operations (Paluszny et al., 2020). Additionally, the production of brine and small amounts of oil during the CPG stage creates voidage, expanding the pore space, thereby increasing the reservoir's CO_2 storage capacity.

The net CO_2 utilization factors for the EOR stage, observed in this study, align well with field-reported values of 2–4 barrels of oil per ton of CO_2 sequestered (Farajzadeh et al., 2020). For the first time, this study presents net CO_2 utilization factors for CPG operations following EOR in oil fields (Fig. 13). These results highlight the potential of the integrated EOR-CPG system to improve overall energy yields from CO_2 utilization while simultaneously enhancing CO_2 sequestration.

It is important to note that this study is based on simulations of "layer-cake" heterogeneous models. Reservoir connectivity and cross-flow dynamics could vary significantly in alternative geometries, such as steeply dipping formations, potentially influencing CO_2 plume behavior. Therefore, future uncertainty assessments should explore the impact of formation dip angles on CO_2 plume dynamics during post-EOR CPG operations.

In addition, the suitability of reservoirs for post-EOR CPG operations depends strongly on their geological and thermal characteristics. Our simulations assumed "typical" oil reservoirs suitable for CO_2-EOR, with sufficient permeability, connectivity, and net thickness, and without complete vertical barriers such as shale breaks. These assumptions favor effective plume migration and oil and geothermal energy recovery. In practice, candidate reservoirs should combine adequate permeability and connectivity with sufficient thickness, as well as heat-in-place prior to CPG, to support both plume sweep and heat extraction, while avoiding highly fractured settings that may lead to reduced storage. Recognizing these constraints is critical for identifying reservoirs with the greatest potential for successful CPG deployment.

4.3.3. Additional oil recovery during CPG

Another notable outcome of implementing CPG after EOR is the recovery of co-produced oil over extended operational periods, even though the primary production fluid is CO_2. This incremental oil production arises as a byproduct of continued CO_2 injection and can be considered a secondary benefit of the CPG process.

In this study, however, we excluded this additional oil from the energy calculations. This choice reflects the assumption of a full transition away from fossil fuel use and ensures a clear comparison between the chemical energy of oil produced during EOR and the thermal energy generated during CPG. By isolating the geothermal contribution of CPG, we provide a focused evaluation of its effectiveness as a standalone energy recovery process. Future work could explore the implications of this co-produced oil in terms of its economic value, lifecycle CO_2 emissions, and potential impact on overall system efficiency.

5. Conclusions

This study examines the integration of CO_2-Plume Geothermal (CPG) energy production with CO_2-Enhanced Oil Recovery (CO_2-EOR) in mature oil reservoirs, extending CO_2 circulation and sequestration beyond the typical EOR lifespan. Heterogeneous reservoir models were simulated to assess the additional energy yield and enhanced CO_2

sequestration resulting from this EOR-CPG approach, and the findings demonstrate that coupling CO_2-EOR with CPG substantially increases energy recovery and broadens the potential for permanent geologic CO_2 storage. The following conclusions can be drawn:

- Initiating CPG operations after CO_2-EOR takes advantage of the established CO_2 plume, enabling immediate and efficient geothermal energy extraction. Because native reservoir fluids (oil and brine) are largely displaced during EOR and the plume stabilizes with continued injection, reservoir heterogeneity has a stronger effect on final oil recovery than on post-EOR CPG performance.
- Under typical operational parameters (Section 2.3), CPG yields thermal power outputs of 13–23 MW_{th} per 1 km^2, based on a single 1 km^2 inverted five-spot well pattern. Power decline rates range from 6% to over 40%, with an average decline of 24% after injecting 10 pore volumes of CO_2 in the CPG stage.
- CPG provides 20%–50% additional energy compared to the chemical energy recovered during EOR. When scaled to a full-field scenario, this integrated CPG-EOR system could deliver substantial clean energy while extending the productive life of mature oil fields.
- Continued CO_2 injection during CPG allows the CO_2 plume to access previously unswept regions, increasing total CO_2 sequestration by 80%–280% compared to EOR alone.
- Heat depletion during CPG further enhances CO_2 storage by increasing its in-situ density, allowing 9%–20% additional CO_2 mass to be stored per unit reservoir volume.
- Net CO_2 utilization factors stabilize near the end of EOR at 2.5 – 3.5 bbl/tCO_2, while the net CO_2 utilization factor during CPG spans from approximately 0.7 to over 2.4 MW_{th}h per ton of CO_2 sequestered.

These findings show that integrating CO_2-EOR with CPG creates a pathway to large-scale CCUS deployment by adding value through geothermal energy production in mature oil fields. This "geothermal" component can offset energy-intensive processes, such as CO_2 separation, compression, and transport—particularly important in remote or offshore environments. Moreover, implementing CPG after EOR supports long-term decarbonization targets by transforming emitted CO_2 from waste into a valuable economic and energy resource, while deferring decommissioning costs and offering both environmental and economic advantages.

CRediT authorship contribution statement

S. Kucuk: Writing – review & editing, Writing – original draft, Visualization, Validation, Methodology, Investigation, Formal analysis, Data curation, Conceptualization. **R. Farajzadeh:** Writing – review & editing, Methodology, Conceptualization. **M. Brehme:** Writing – review & editing, Supervision, Project administration, Methodology, Conceptualization. **W.R. Rossen:** Writing – review & editing, Methodology, Conceptualization. **M.O. Saar:** Writing – review & editing, Supervision, Project administration, Methodology, Conceptualization.

Declaration of competing interest

The authors declare that they have no known competing financial interests or personal relationships that could have appeared to influence the work reported in this paper.

Acknowledgments

The corresponding author acknowledges the financial support provided by the Ministry of Education of the Republic of Türkiye during the PhD program.

We gratefully acknowledge the support of the Werner Siemens Foundation (Werner Siemens-Stiftung) for its support of the Geothermal Energy and Geofluids (GEG.ethz.ch) group at ETH Zurich. Additionally, we appreciate the support of the Energi Simulation Foundation. We also extend our gratitude to Computer Modeling Group Ltd. for supplying the GEM and COFLOW software packages and for their valuable support throughout the simulation phase of this study.

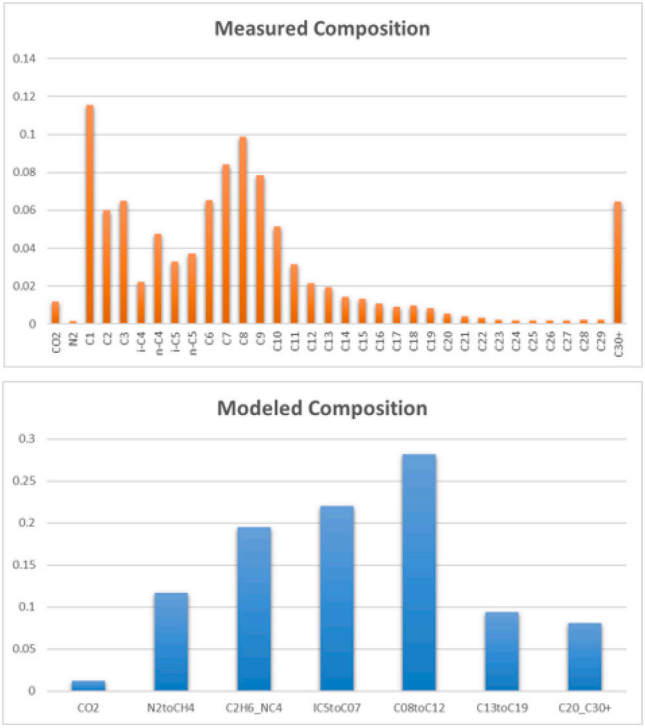

Fig. A.14. (a) Composition of the reservoir oil (b) pseudo-components modeled for the simulations.

Appendix A. Fluid modeling

In this study, the oil composition used for simulations is based on data from a major oil field in the Middle East (Al-Mudhafar et al., 2022), as depicted in Fig. A.14. The key phase properties of the EOS-oil model are summarized in Table A.4.

Appendix B. Relative permeability curves

The relative permeability curves for water-oil and gas-liquid systems used in the simulations are presented in Fig. B.15. The oil relative permeability in the three-phase system is calculated using a modified version of Stone's second model (Aziz and Settari, 1979). Capillary pressure and hysteresis effects are not considered in this study.

Appendix C. Wellbore modeling

Reservoir simulations for this study were carried out using GEM (Computer Modeling Group, 2024b). However, GEM does not natively incorporate wellbore modeling capabilities. To account for the multiphase, multicomponent flow in the wellbore, we utilized the nodal analysis feature of CoFlow (Computer Modeling Group, 2024a) to generate pressure and temperature profiles along the wellbores. These profiles were derived based on the results of the GEM simulations.

The production bottomhole pressure (BHP) is a key simulation constraint, as detailed in Section 2.3.4, and is held constant throughout the simulation. Meanwhile, the bottomhole temperature (BHT) is dynamically calculated by GEM, reflecting reservoir heat depletion over time. Given that the BHT decreases with reservoir heat depletion, the

Table A.4
Pseudo-component properties of the EOS oil model used in the simulations under initial reservoir conditions.

Component	Mole (%)	Pc (Atm)	Tc (°K)	Acentric factor	Molecular weight	Omega A	Omega B	Specific gravity
CO_2	1.18	72.8	304.2	0.225	44.01	0.4572	0.078	0.818
N_2toCH_4	11.70	45.2	189.7	0.008	16.21	0.4572	0.078	0.305
C_2H_6toNC_4	19.45	43.5	411.9	0.148	44.79	0.5487	0.062	0.492
IC_5toC_7	22.03	37.7	556.9	0.249	83.46	0.4572	0.078	0.701
C_8toC_{12}	28.15	28.1	667.2	0.328	120.5	0.4572	0.078	0.792
C_{13}toC_{19}	9.40	23.4	673.5	0.568	210.7	0.4572	0.078	0.847
C_{20}toC_{30+}	8.09	15.4	792.8	0.942	309.9	0.4572	0.078	0.935

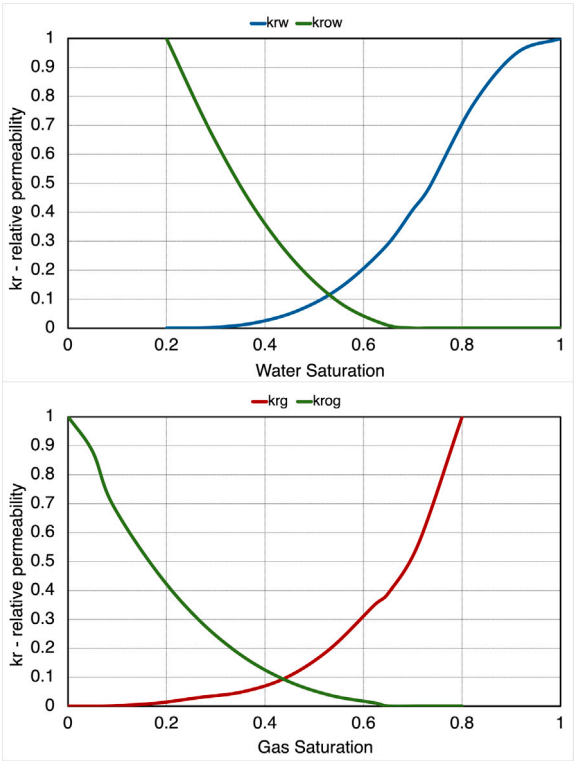

Fig. B.15. Relative permeability curves used in the simulations.

fluid density and pressure profiles within the wellbore also evolve. Consequently, the wellhead pressure (WHP) varies with changes in fluid temperature.

Figs. C.16 and C.17 illustrate the results of our wellbore simulations and subsequent data processing.

Fig. C.16 shows the pressure and temperature profiles along the injection and production wellbores under varying conditions:

- **Subplot (a):** Pressure profiles along the CO_2 injection well for different bottomhole pressures. These profiles are used to calculate the injector WHP, which is necessary for determining the injection fluid's specific enthalpy at the surface. The bottomhole pressure values represent a range that meets the mass flow constraints defined in the GEM simulations (see Section 2.3.4).
- **Subplot (b):** Temperature profiles along the production wellbore for varying bottomhole temperatures.
- **Subplot (c):** Pressure profiles for the production wellbore at constant BHP, corresponding to the BHT values shown in subplot (b) (same color coding is used), illustrating how pressure change with varying BHT.

Using the simulated pressure and temperature profiles, we generated a lookup table to couple the reservoir simulation results from GEM with the wellbore models during post-processing. This lookup table facilitates the calculation of WHP and wellhead temperature (WHT) for varying BHP and BHT conditions. These surface parameters are critical for determining the specific enthalpy of the CO_2 at the wellhead, which is used to estimate the gross power output of the CPG system.

Fig. C.17 illustrates the final processed values included in the lookup table, demonstrating the relationship between BHP, BHT, WHP, and WHT.

Appendix D. Wellhead enthalpies and production mass rates

The calculated pressure and temperature of the production and injection fluids at surface conditions, as detailed in Appendix C, were used to determine the wellhead specific enthalpies (assuming 100% CO_2) presented in Fig. D.18 using CoolProp (Bell et al., 2014).

Appendix E. Track of CO_2 plume density on a P-T diagram

The mean density of the CO_2 plume is shown on a pressure–temperature diagram for the two example models. The sharp increase at the transition from EOR to CPG results from raising the CO_2 injection rate from 0.1 to 0.5 PV/year to maximize thermal output, which leads

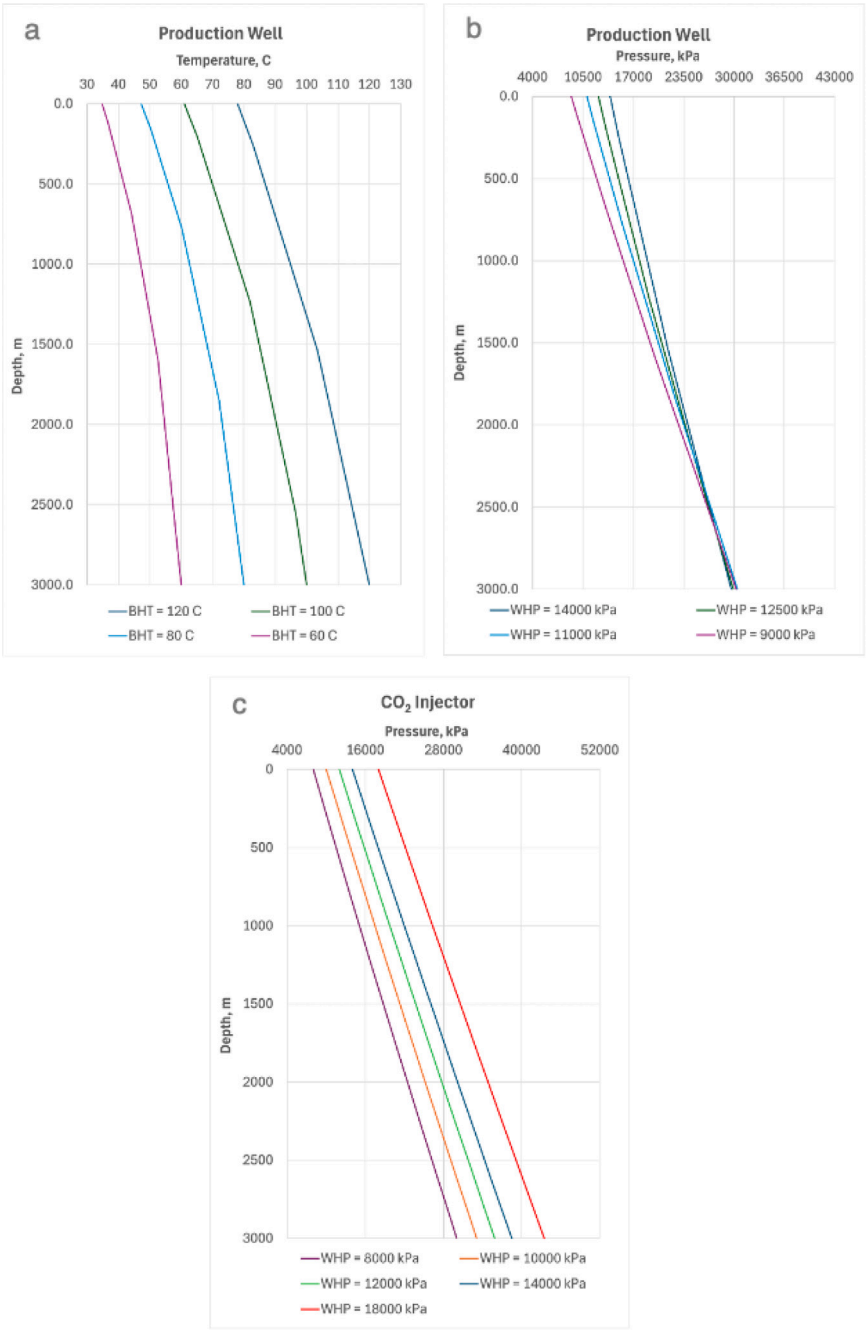

Fig. C.16. Wellbore simulation results. (a) Temperature profiles along the production wellbore for varying bottomhole temperatures. (b) Pressure profiles along the production wellbore corresponding to the same conditions in (a). (c) Pressure profiles along the CO_2 injection well for varying bottomhole pressures.

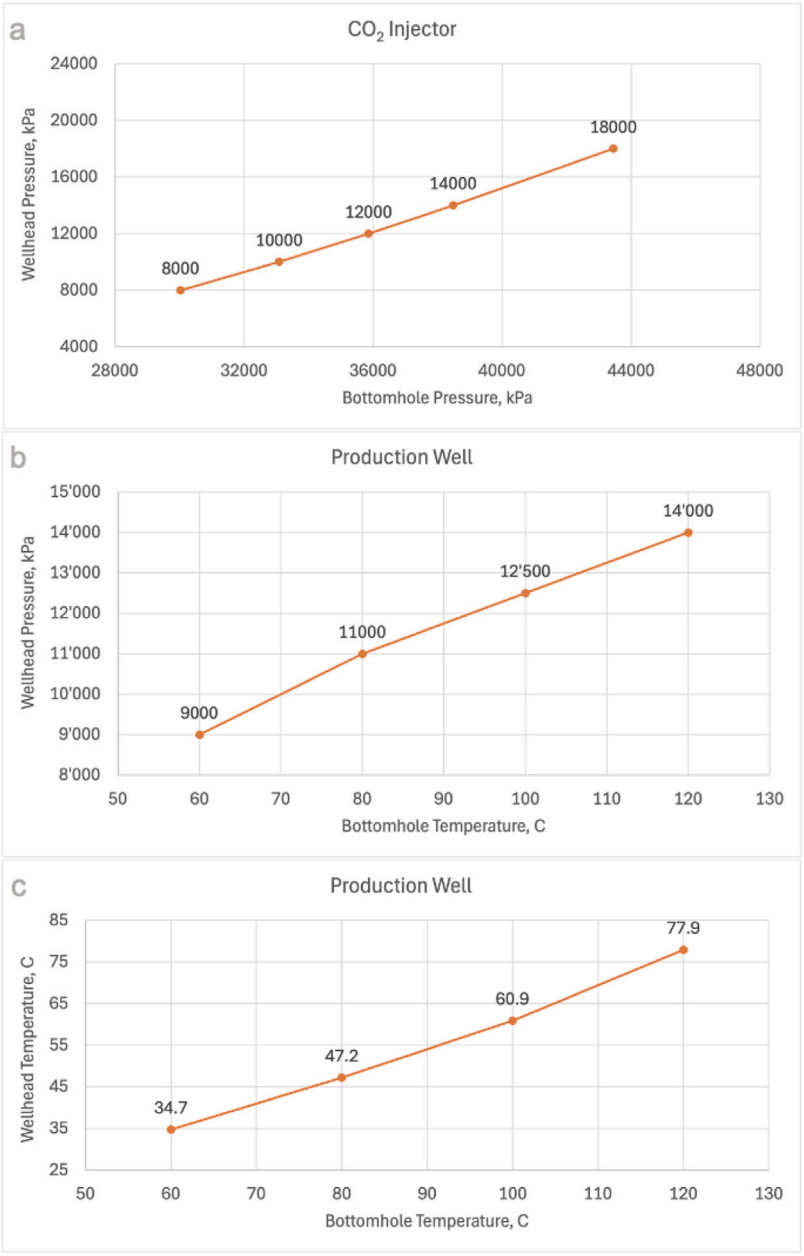

Fig. C.17. Lookup table values for varying bottomhole pressures and temperatures. The table provides corresponding wellhead pressures and temperatures, used in post-processing to estimate CO_2 specific enthalpy and gross power output.

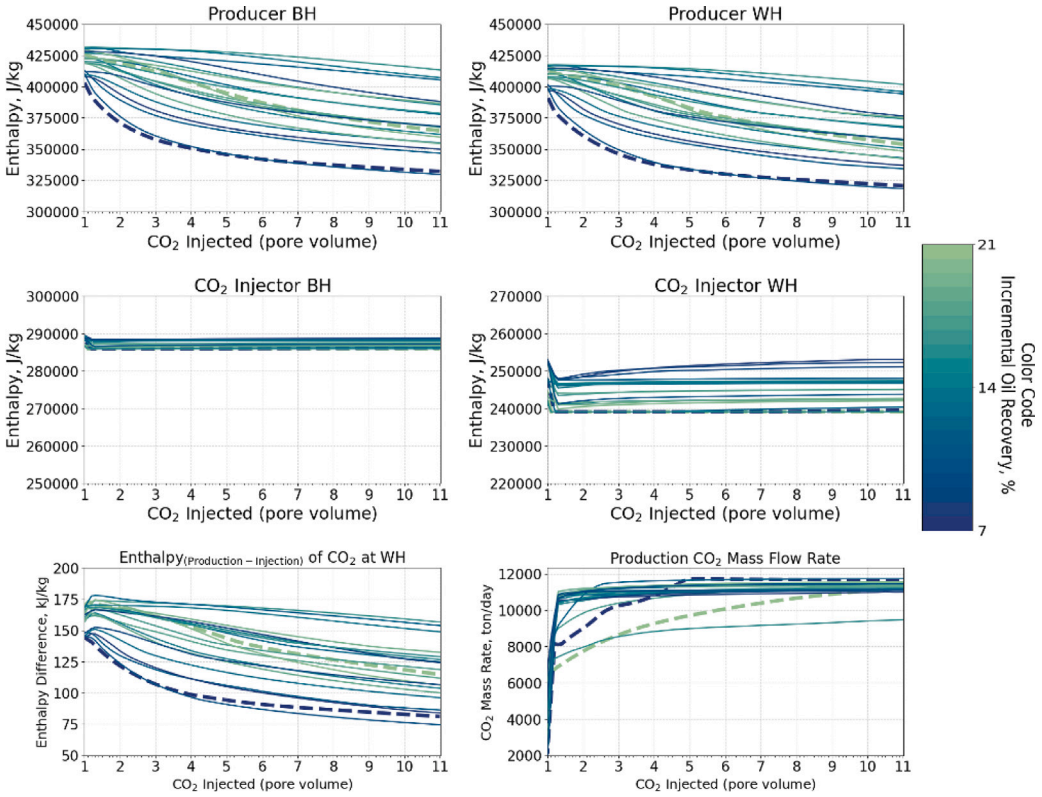

Fig. D.18. Variation in enthalpy and CO_2 production metrics with CO_2 injected (in pore volumes) across multiple operating conditions. The top row shows enthalpy profiles at the producer bottomhole (BH) and wellhead (WH) as a function of incremental oil recovery (color-coded). The middle row presents enthalpy trends at the CO_2 injector bottomhole (BH) and wellhead (WH). The bottom row highlights the enthalpy difference between production and injection at the CO_2 wellhead (left) and the CO_2 production mass flow rate (right).

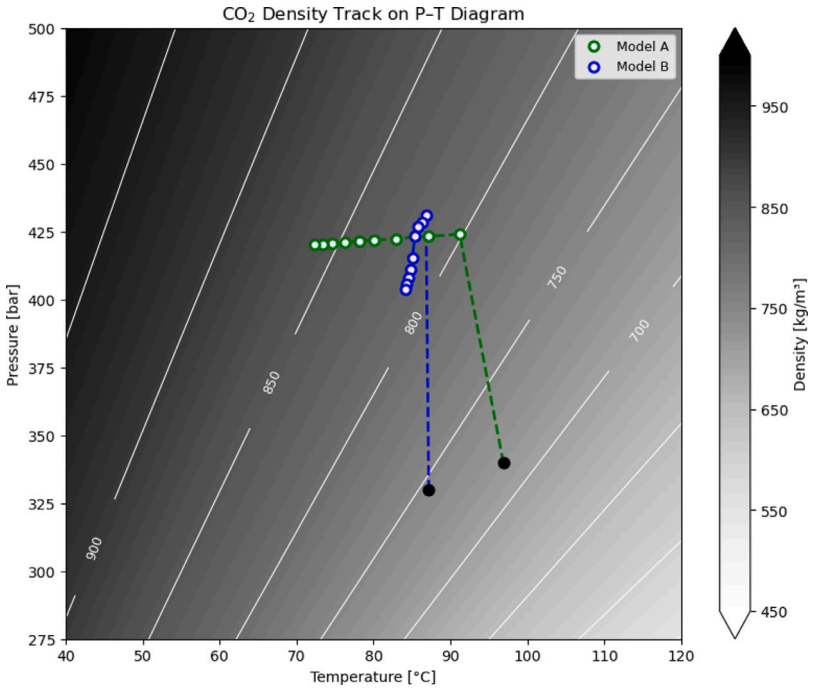

Fig. E.19. CO_2 plume density on a P–T diagram for Models A and B. Black markers indicate plume density at the end of EOR, while blue and green markers track density evolution during CPG.

to higher injection pressures and thus higher plume density. During the CPG stage, Model A shows a gradual density increase due to reservoir cooling. In contrast, plume density in Model B remains nearly constant, or even decreases slightly, because the CO_2 continues sweeping previously bypassed regions more effectively (see Fig. 12), which mitigates cooling of the overall plume. Nonetheless, local cooling and associated density increases are still observed in the simulations.

Data availability

Data will be made available on request.

References

Adams, B.M., Kuehn, T.H., Bielicki, J.M., Randolph, J.B., Saar, M.O., 2014. On the importance of the thermosiphon effect in CPG (CO2 plume geothermal) power systems. Energy 69, 409–418. http://dx.doi.org/10.1016/j.energy.2014.03.032.

Adams, B.M., Kuehn, T.H., Bielicki, J.M., Randolph, J.B., Saar, M.O., 2015. A comparison of electric power output of CO2 plume geothermal (CPG) and brine geothermal systems for varying reservoir conditions. Appl. Energy 140, 365–377. http://dx.doi.org/10.1016/j.apenergy.2014.11.043.

Adams, B.M., Vogler, D., Kuehn, T.H., Bielicki, J.M., Garapati, N., Saar, M.O., 2021. Heat depletion in sedimentary basins and its effect on the design and electric power output of CO2 plume geothermal (CPG) systems. Renew. Energy 172, 1393–1403. http://dx.doi.org/10.1016/j.renene.2020.11.145.

Ahmed, T., 2007. Equations of State and PVT Analysis: Applications for Improved Reservoir Modeling. Gulf Publishing Company, Houston, Texas.

Al-Mudhafar, W.J., Rao, D.N., Srinivasan, S., Thanh, H.V., Lawe, E.M.A., 2022. Rapid evaluation and optimization of carbon dioxide-enhanced oil recovery using reduced-physics proxy models. Energy Sci. Eng. 10, 4112–4135. http://dx.doi.org/10.1002/ese3.1276.

Alvarado, V., Manrique, E., 2010. Enhanced oil recovery: An update review. Energies 3, 1529–1575. http://dx.doi.org/10.3390/en3091529.

Ampomah, W., Balch, R.S., Cather, M., Will, R., Gunda, D., Dai, Z., Soltanian, M.R., 2017. Optimum design of CO2 storage and oil recovery under geological uncertainty. Appl. Energy 195, 80–92. http://dx.doi.org/10.1016/j.apenergy.2017.03.017.

Atrens, A.D., Gurgenci, H., Rudolph, V., 2009. CO2 thermosiphon for competitive geothermal power generation. Energy Fuels 23, 553–557. http://dx.doi.org/10.1021/ef800601z.

Aycaguer, A.C., Lev-On, M., Winer, A.M., 2001. Reducing carbon dioxide emissions with enhanced oil recovery projects: A life cycle assessment approach. Energy Fuels 15, 303–308. http://dx.doi.org/10.1021/ef000258a.

Aziz, K., Settari, A., 1979. Petroleum Reservoir Simulation. Society of Petroleum Engineers, http://dx.doi.org/10.2118/9781613999646.

Azzolina, N.A., Nakles, D.V., Gorecki, C.D., Peck, W.D., Ayash, S.C., Melzer, L.S., Chatterjee, S., 2015. CO2 storage associated with CO2 enhanced oil recovery: A statistical analysis of historical operations. Int. J. Greenh. Gas Control. 37, 384–397. http://dx.doi.org/10.1016/j.ijggc.2015.03.037.

Bell, I.H., Wronski, J., Quoilin, S., Lemort, V., 2014. Pure and pseudo-pure fluid thermophysical property evaluation and the open-source thermophysical property library coolprop. Ind. Eng. Chem. Res. 53, 2498–2508. http://dx.doi.org/10.1021/ie4033999.

Bennett, J., Schmidt, K.A., 2017. Comparison of phase identification methods used in oil industry flow simulations. Energy Fuels 31, 3370–3379. http://dx.doi.org/10.1021/acs.energyfuels.6b02316.

Brown, D.W., 2000. A hot dry rock geothermal energy concept utilizing supercritical CO2 instead of water. In: PROCEEDINGS, Twenty-Fifth Workshop on Geothermal Reservoir Engineering. Stanford, California.

Christiensen, J.R., Stenby, E.H., Skauge, A., 2001. Review of WAG field experience. SPE Reserv. Eval. Eng..

Collins, D.A., Nghlem, L.X., Li, Y.-K., Grabenstetter, J.E., 1992. An efficient approach to adaptive-implicit compositional simulation with an equation of state. SPE Reserv. Eng..

Computer Modeling Group, 2024a. Coflow user's manual. URL www.cmgl.ca.

Computer Modeling Group, 2024b. GEM user's manual. URL www.cmgl.ca.

Computer Modeling Group, 2024c. WinProp user's manual. URL www.cmgl.ca.

Cui, G., Zhang, L., Ren, B., Enechukwu, C., Liu, Y., Ren, S., 2016. Geothermal exploitation from depleted high temperature gas reservoirs via recycling supercritical CO2: Heat mining rate and salt precipitation effects. Appl. Energy 183, 837–852. http://dx.doi.org/10.1016/j.apenergy.2016.09.029.

Erdlac, R.J., Armour, L., Lee, R., Snyder, S., Sorensen, M., Matteucci, M., Horton, J., 2007. Ongoing resource assessment of geothermal energy from sedimentary basins in texas. In: PROCEEDINGS, Thirty-Second Workshop on Geothermal Reservoir Engineering. Stanford, California.

Esteves, A.F., Santos, F.M., Pires, J.C.M., 2019. Carbon dioxide as geothermal working fluid: An overview. Renew. Sustain. Energy Rev. 114, http://dx.doi.org/10.1016/j.rser.2019.109331.

Ezekiel, J., Ebigbo, A., Adams, B.M., Saar, M.O., 2020. Combining natural gas recovery and CO2-based geothermal energy extraction for electric power generation. Appl. Energy 269, http://dx.doi.org/10.1016/j.apenergy.2020.115012.

Farajzadeh, R., Eftekhari, A.A., Dafnomilis, G., Lake, L.W., Bruining, J., 2020. On the sustainability of CO2 storage through CO2 – enhanced oil recovery. Appl. Energy 261, http://dx.doi.org/10.1016/j.apenergy.2019.114467.

Garapati, N., Randolph, J.B., Saar, M.O., 2015. Brine displacement by CO2, energy extraction rates, and lifespan of a CO2-limited CO2-plume geothermal (CPG) system with a horizontal production well. Geothermics 55, 182–194. http://dx.doi.org/10.1016/j.geothermics.2015.02.005.

Garapati, N., Randolph, J.B., Valencia, J.L., Saar, M.O., 2014. CO2-plume geothermal (CPG) heat extraction in multi-layered geologic reservoirs. In: Energy Procedia. vol. 63, Elsevier Ltd, pp. 7631–7643. http://dx.doi.org/10.1016/j.egypro.2014.11.797.

Gosset, R., Heyen, G., Kalitventzeff, B., 1986. An efficient algorithm to solve cubic equations of state. Fluid Phase Equilib. 25, 51–64. http://dx.doi.org/10.1016/0378-3812(86)85061-0.

Gray, H.E., 1978. Vertical Flow Correlation in Gas Wells. User's Manual for API 14B Surface Controlled Subsurface Safety Valve Sizing Computer Program. Tech. rep., American Petroleum Institute, Dallas.

Hamouda, A.A., Bagalkot, N., 2019. Effect of salts on interfacial tension and CO2 mass transfer in carbonated water injection. Energies 12, http://dx.doi.org/10.3390/en12040748.

Harvey, A.H., 1996. Semiempirical correlation for henry's constants over large temperature ranges. AIChE J. 42, 1491–1494. http://dx.doi.org/10.1002/aic.690420531.

Hau, K.P., Brehme, M., Shokri, A.R., Malakooti, R., Nickel, E., Chalaturnyk, R.J., Saar, M.O., 2025. CCS coupled with CO2 plume geothermal operations: Enhancing CO2 sequestration and reducing risks. Geothermics 133, 103447. http://dx.doi.org/10.1016/j.geothermics.2025.103447.

Holm, L.W., Josendal, V.A., 1974. Mechanisms of oil displacement by carbon dioxide. J. Pet. Technol..

Honarpour, M.M., Nagarajan, N.R., Grijalba, A.C., Valle, M., Adesoye, K., 2010. Rock-fluid characterization for miscible CO2 injection: Residual oil zone, seminole field, permian basin. In: SPE Annual Technical Conference and Exhibition. Society of Petroleum Engineers, Florence, Italy, pp. 19–22.

Hosseininoosheri, P., Hosseini, S.A., Nuñez-López, V., Lake, L.W., 2018. Impact of field development strategies on CO2 trapping mechanisms in a CO2–EOR field: A case study in the permian basin (SACROC unit). Int. J. Greenh. Gas Control. 72, 92–104. http://dx.doi.org/10.1016/j.ijggc.2018.03.002.

Huang, Y., Cheng, Y., Ren, L., Tian, F., Pan, S., Wang, K., Wang, J., Dong, Y., Kong, Y., 2022. Assessing the geothermal resource potential of an active oil field by integrating a 3D geological model with the hydro-thermal coupled simulation. Front. Earth Sci. 9, http://dx.doi.org/10.3389/feart.2021.787057.

IEA, 2015. Storing CO2 through Enhanced Oil Recovery Combining EOR with CO2 storage (EOR+) for profit. Tech. rep..

IEA, 2021. Net Zero by 2050 - A Roadmap for the Global Energy Sector. Tech. rep., International Energy Agency, Paris, URL www.iea.org/t&c/.

Institute, G.C., 2021. Global Status of CCS 2021 - CCS Accelerating to Net Zero. Tech. rep..

IPCC, 2022. Climate Change 2022 - Mitigation of Climate Change. Tech. rep., Intergovernmental Panel on Climate Change, Cambridge and New York, http://dx.doi.org/10.1017/9781009157926.001, URL www.ipcc.ch.

Johns, R.T., Dindoruk, B., 2013. Gas flooding. In: Sheng, J. (Ed.), Enhanced Oil Recovery Field Case Studies. Elsevier.

Jossi, J.A., Stiel, L.I., Thodos, G., 1962. The viscosity of pure substances in the dense gaseous and liquid phases. AIChE J. 8, 59–63. http://dx.doi.org/10.1002/aic.690080116.

Karimov, D., Toktarbay, Z., 2024. Enhanced oil recovery: Techniques, strategies, and advances. ES Mater. Manuf. 23, http://dx.doi.org/10.30919/esmm1005.

Kestin, J., Khalifa, H.E., Correia, R.J., 1981. Tables of the dynamic and kinematic viscosity of aqueous NaCl solutions in the temperature range 20-150 °C and the pressure range 0.1-35 MPa. J. Phys. Chem. Ref. Data 10, 71–88. http://dx.doi.org/10.1063/1.555641.

Khan, M.Y., Mandal, A., 2021. The impact of permeability heterogeneity on water-alternating-gas displacement in highly stratified heterogeneous reservoirs. J. Pet. Explor. Prod. Technol. 12, 871–897. http://dx.doi.org/10.1007/s13202-021-01347-3.

Kharseh, M., Al-Khawaja, M., Hassani, F., 2015. Utilization of oil wells for electricity generation: Performance and economics. Energy 90, 910–916. http://dx.doi.org/10.1016/j.energy.2015.07.116.

Koperna, G., Inc, A.R.I., Melzer, L., Consulting, M., Kuuskraa, V., 2006. Recovery of oil resources from the residual and transitional oil zones of the permian basin. In: SPE Annual Technical Conference and Exhibition. Society of Petroleum Engineers, San Antonio, Texas.

Kutsienyo, E.J., Appold, M.S., White, M.D., Ampomah, W., 2021. Numerical modeling of CO2 sequestration within a five-spot well pattern in the morrow b sandstone of the farnsworth hydrocarbon field: Comparison of the TOUGHREACT, STOMP-EOR, and GEM simulators. Energies 14, http://dx.doi.org/10.3390/en14175337.

Lake, L.W., Johns, R., Rossen, B., 2014. Fundamentals of Enhanced Oil Recovery. SPE, p. 622.
Lake, L.W., Lotfollahi, M., Bryant, S.L., 2018. Fifty years of field observations: Lessons for CO 2 storage from CO2 enhanced oil recovery. In: 14th International Conference on Greenhouse Gas Control Technologies. Melbourne.
Lake, L.W., Lotfollahi, M., Bryant, S.L., 2019. CO2 enhanced oil recovery experience and its messages for CO2 storage. In: Science of Carbon Storage in Deep Saline Formations: Process Coupling Across Time and Spatial Scales. Elsevier, pp. 15–31. http://dx.doi.org/10.1016/B978-0-12-812752-0.00002-2.
Lee, S., Kam, S.I., 2013. Enhanced oil recovery by using CO2 foams: Fundamentals and field applications. In: Sheng, J. (Ed.), Enhanced Oil Recovery Field Case Studies. Elsevier.
Li, H., Lu, C., Werner, A.D., Irvine, D.J., Luo, J., 2022. Impacts of heterogeneity on aquifer storage and recovery in saline aquifers. Water Resour. Res. 58, http://dx.doi.org/10.1029/2021WR031306.
Li, T., Zhu, J., Xin, S., Zhang, W., 2014. A novel geothermal system combined power generation, gathering heat tracing, heating/domestic hot water and oil recovery in an oilfield. Geothermics 51, 388–396. http://dx.doi.org/10.1016/j.geothermics.2014.03.009.
Liu, X., Falcone, G., Alimonti, C., 2018. A systematic study of harnessing low-temperature geothermal energy from oil and gas reservoirs. Energy 142, 346–355. http://dx.doi.org/10.1016/j.energy.2017.10.058.
Lyons, W.C., Plisga, G.J., Lorenz, M.D., 2016. General engineering and science. In: Lyons, W.C., Plisga, G.J., Lorenz, M.D. (Eds.), Standard Handbook of Petroleum and Natural Gas Engineering. Elsevier, pp. 102–107. http://dx.doi.org/10.1016/b978-0-12-383846-9.00002-3.
Massarweh, O., Abushaikha, A.S., 2022. A review of recent developments in CO2 mobility control in enhanced oil recovery. Petroleum 8, 291–317. http://dx.doi.org/10.1016/j.petlm.2021.05.002.
Milliken, M., 2007. Geothermal resources at naval petroleum reserve-3 (npr-3), wyoming. In: PROCEEDINGS, Thirty-Second Workshop on Geothermal Reservoir Engineering. Stanford, California.
Morrow, N.R., 1990. Wettability and its effect on oil recovery. J. Pet. Technol..
Nazarian, B., Furre, A.-K., Asa, E., 10, A.E.V., Rotvoll, N., 2022. Simulation study of sleipner plume on entire utsira using a multi-physics modelling approach. In: 16th International Conference on Greenhouse Gas Control Technologies. Lyon, France, URL https://ssrn.com/abstract=4274191.
Nghiem, L., Sammon, P., Grabenstetter, J., Ohkuma, H., 2004. Modeling CO2 storage in aquifers with a fully-coupled geochemical eos compositional simulator. In: SPE/DOE Fourteenth Symposium on Improved Oil Recovery. Society of Petroleum Engineers, Tulsa, Oklahoma.
Nick, H.M., Schotting, R., Gutierrez-Neri, M., Johannsen, K., 2009. Modeling transverse dispersion and variable density flow in porous media. Transp. Porous Media 78, 11–35. http://dx.doi.org/10.1007/s11242-008-9277-x.
Norouzi, A.M., Gluyas, J., Babaei, M., 2022. CO2-plume geothermal in fluvial formations: A 2D numerical performance study using subsurface metrics and upscaling. Geothermics 99, http://dx.doi.org/10.1016/j.geothermics.2021.102287.
Norouzi, A.M., Pouranian, F., Rabbani, A., Fowler, N., Gluyas, J., Niasar, V., Ezekiel, J., Babaei, M., 2023. CO2-plume geothermal: Power net generation from 3D fluvial aquifers. Appl. Energy 332, http://dx.doi.org/10.1016/j.apenergy.2022.120546.
Núñez-López, V., Moskal, E., 2019. Potential of CO2-EOR for near-term decarbonization. Front. Clim. 1, http://dx.doi.org/10.3389/fclim.2019.00005.
Orr, F.M., 2018. Carbon capture, utilization, and storage: An update. SPE J. 23, 2444–2455. http://dx.doi.org/10.2118/194190-PA.
Paluszny, A., Graham, C.C., Daniels, K.A., Tsaparli, V., Xenias, D., Salimzadeh, S., Whitmarsh, L., Harrington, J.F., Zimmerman, R.W., 2020. Caprock integrity and public perception studies of carbon storage in depleted hydrocarbon reservoirs. Int. J. Greenh. Gas Control. 98, http://dx.doi.org/10.1016/j.ijggc.2020.103057.
Pan, F., McPherson, B.J., Esser, R., Xiao, T., Appold, M.S., Jia, W., Moodie, N., 2016. Forecasting evolution of formation water chemistry and long-term mineral alteration for GCS in a typical clastic reservoir of the Southwestern United States. Int. J. Greenh. Gas Control. 54, 524–537. http://dx.doi.org/10.1016/j.ijggc.2016.07.035.
Pedersen, K.S., Christensen, P.L., Shaikh, J.A., 2015. Phase Behavior of Petroleum Reservoir Fluids. CRC Press.
Peng, D.-Y., Robinson, D.B., 1976. A new two-constant equation of state. Ind. Eng. Chem. Fundam. 15, URL https://pubs.acs.org/sharingguidelines.
Pruess, K., 2006. Enhanced geothermal systems (EGS) using CO2 as working fluid - a novel approach for generating renewable energy with simultaneous sequestration of carbon. Geothermics 35, 351–367. http://dx.doi.org/10.1016/j.geothermics.2006.08.002.
Pruess, K., Azaroual, M., 2006. On The Feasibility Of Using Supercritical Co2 As Heat Transmission Fluid In An Engineered Hot Dry Rock Geothermal System. Tech. rep..
Randolph, J.B., Saar, M.O., 2011. Combining geothermal energy capture with geologic carbon dioxide sequestration. Geophys. Res. Lett. 38, n/a–n/a. http://dx.doi.org/10.1029/2011gl047265.
Rangel-Jurado, N., Hawkins, A.J., Fulton, P.M., 2023. Influence of extreme fracture flow channels on the thermal performance of open-loop geothermal systems at commercial scale. Geotherm. Energy 11, http://dx.doi.org/10.1186/s40517-023-00261-7.
Rangel-Jurado, N., Kong, X.Z., Kottsova, A., Morales, L.G., Ma, N., Games, F., Brehme, M., Bernasconi, S.M., Saar, M.O., 2025. Reactivity of wet scCO2 toward reservoir and caprock formations under elevated pressure and temperature conditions: Implications for CCS and CO2-based geothermal energy extraction. Energy Fuels http://dx.doi.org/10.1021/acs.energyfuels.4c04515.
Rangel-Jurado, N., Küçük, S., Brehme, M., Lathion, R., Games, F., Saar, M.O., 2022. Comparative analysis on the techno-economic performance of different types of deep geothermal systems for heat production. In: European Geothermal Congress. Berlin, URL https://www.researchgate.net/publication/368478089.
Räss, L., Kolyukhin, D., Minakov, A., 2019. Efficient parallel random field generator for large 3-D geophysical problems. Comput. Geosci. 131, 158–169. http://dx.doi.org/10.1016/j.cageo.2019.06.007.
Ren, B., Duncan, I., 2019. Modeling oil saturation evolution in residual oil zones: Implications for CO2 EOR and sequestration. J. Pet. Sci. Eng. 177, 528–539. http://dx.doi.org/10.1016/j.petrol.2019.02.072.
Robin, M.J., Gutjahr, A.L., Sudicky, E.A., Wilson, J.L., 1993. Cross-correlated random field generation with the direct Fourier transform method. Water Resour. Res. 29, 2385–2397. http://dx.doi.org/10.1029/93WR00386.
Rowe, A.M., Chou, J.C.S., 1970. Pressure-volume-temperature-concentration relation of aqueous naci solutions. J. Chem. Eng. Data 15.
Schifflechner, C., de Reus, J., Schuster, S., Villasana, A.C., Brillert, D., Saar, M.O., Spliethoff, H., 2024. Paving the way for CO2-plume geothermal (CPG) systems: A perspective on the CO2 surface equipment. Energy 305, http://dx.doi.org/10.1016/j.energy.2024.132258.
Sheth, S., Bennett, J., Kachuma, D., Heidari, M.R., Shaykhattarov, M., 2023. A new phase-labeling method based on machine learning for CO2 applications. In: Society of Petroleum Engineers - SPE Reservoir Simulation Conference, RSC 2023. Society of Petroleum Engineers, http://dx.doi.org/10.2118/212254-MS.
Shmeleva, M., 2018. Geothermal Energy Production from Oil and Gas Wells (Ph.D. thesis). Division of Heat and Power Technology, Stockholm.
Singh, H.K., 2020. Geothermal energy potential of Indian oilfields. Geomech. Geophys. Geo-Energy Geo-Resources 6, http://dx.doi.org/10.1007/s40948-020-00148-y.
Soldo, E., Alimonti, C., Scrocca, D., 2020. Geothermal repurposing of depleted oil and gas wells in Italy. In: Proceedings - First World Energies Forum. MDPI AG, http://dx.doi.org/10.3390/wef-06907.
Stalkup, F.I., 1983. Status of miscible displacement. J. Pet. Technol..
Taheriotaghsara, M., Hosseinzadehsadati, S., Nick, H.M., 2020. The impact of spatially correlated heterogeneity and adsorption on modified salinity water in carbonates. ACS Omega 5, 29780–29794. http://dx.doi.org/10.1021/acsomega.0c03679.
Thompson, N., Andrews, J.S., Wu, L., Meneguolo, R., 2022. Characterization of the in-situ stress on the horda platform – a study from the northern lights eos well. Int. J. Greenh. Gas Control. 114, http://dx.doi.org/10.1016/j.ijggc.2022.103580.
Vinsome, P., Westerveld, J., 1980. A simple method for predicting cap and base rock heat losses in thermal reservoir simulations. J. Can. Pet. http://dx.doi.org/10.2118/80-03-04/2167128/petsoc-80-03-04.pdf/1.
Williams, G.A., Chadwick, R.A., 2017. An improved history-match for layer spreading within the sleipner plume including thermal propagation effects. In: Energy Procedia. vol. 114, Elsevier Ltd, pp. 2856–2870. http://dx.doi.org/10.1016/j.egypro.2017.03.1406.
Williams, G.A., Chadwick, R.A., 2021. Influence of reservoir-scale heterogeneities on the growth, evolution and migration of a CO2 plume at the Sleipner field, Norwegian north sea. Int. J. Greenh. Gas Control. 106, http://dx.doi.org/10.1016/j.ijggc.2021.103260.
Yoonm, P., Thodos, G., 1970. Viscosity of nonpolar gaseous mixtures at normal pressures. AIChE J. 16, 300–304. http://dx.doi.org/10.1002/aic.690160225.
Zhang, L., Li, D., Ren, B., Cui, G., Zhuang, Y., Ren, S., 2014. Potential assessment of CO2 geological storage in geothermal reservoirs associated with heat mining: Case studies from China. In: Energy Procedia. vol. 63, Elsevier Ltd, pp. 7651–7662. http://dx.doi.org/10.1016/j.egypro.2014.11.799.
Zhang, C., Zhang, L., Wang, X., Rao, S., Zuo, Y., Huang, R., Gao, P., Song, R., Wang, Z., 2021. Effects of the spatial heterogeneity in reservoir parameters on the heat extraction performance forecast based on a 3D thermo-hydro-mechanical coupled model: A case study at the zhacang geothermal field in the guide basin, northeastern tibetan plateau. Geothermics 95, http://dx.doi.org/10.1016/j.geothermics.2021.102161.
Zhong, C., Xu, T., Gherardi, F., Yuan, Y., 2023. Comparison of CO2 and water as working fluids for an enhanced geothermal system in the Gonghe Basin, northwest China. Gondwana Res. 122, 199–214. http://dx.doi.org/10.1016/j.gr.2022.05.014.
Zhu, Y., Li, K., Liu, C., Mgijimi, M.B., 2019. Geothermal power production from abandoned oil reservoirs using in situ combustion technology. Energies 12, http://dx.doi.org/10.3390/en12234476.